

# Solvent Effects on the Menshutkin Reaction

Haydar Taylan Turan,<sup>†</sup> Sebastian Brickel,<sup>†</sup> and Markus Meuwly<sup>\*,†</sup>

<sup>†</sup>*Department of Chemistry, University of Basel, Klingelbergstrasse 80, Basel, Switzerland*

<sup>‡</sup>*Present Address: Department of Chemistry - BMC, Uppsala University, BMC Box 576,  
751 23 Uppsala, Sweden*

E-mail: m.meuwly@unibas.ch

## Abstract

The Menshutkin reaction is a methyl transfer reaction relevant in fields ranging from biochemistry to chemical synthesis. In the present work, energetics and solvent distributions for  $\text{NH}_3 + \text{MeCl}$  and  $\text{Pyr} + \text{MeBr}$  reactions were investigated in the gas-phase, in water, methanol, acetonitrile, benzene, and in cyclohexane by means of reactive molecular dynamics simulations. For polar solvents (water, methanol, and acetonitrile) and benzene, strong to moderate catalytic effect for both reactions is found whereas apolar and bulky cyclohexane interacts weakly with the solute and does not show pronounced barrier reduction. Calculated barrier heights for the  $\text{Pyr} + \text{MeBr}$  reaction in acetonitrile and cyclohexane are 23.2 and 28.1 kcal/mol compared with experimentally measured barriers of 22.5 and 27.6 kcal/mol, respectively. The 2-dimensional solvent distributions change considerably between reactant and TS but comparatively little between TS and product conformations of the solute. The simulations also suggest that as the system approaches the transition state, correlated solvent motions that destabilize the solvent-solvent interactions are required to surmount the barrier. Finally, the average solvent-solvent interaction energies in the reactant, TS, and product state geometries are correlated with changes in the solvent structure around the solute.

# 1 Introduction

Solvation is essential in chemistry and directly influences properties such as reaction rates or spectroscopic responses of solutes.<sup>1-12</sup> Depending on the nature of the solvent (e.g. polar or apolar) the potential energy surface underlying the nuclear dynamics changes and affects mechanistic aspects of the dynamics.<sup>13-15</sup> As an example, for the Claisen rearrangement the reaction barrier in polar solvent decreases compared to the gas phase<sup>16-19</sup> whereas it increases for  $S_N2$  reactions in going from the gas phase into solution.<sup>20-27</sup>

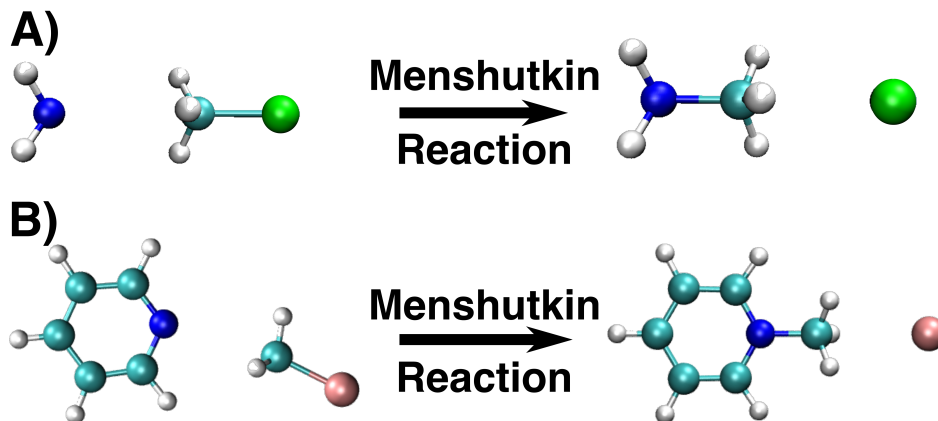


Figure 1: Schematic representation for A) the Menshutkin reaction of ammonia with chloromethane and B) the Menshutkin reaction of pyridine with bromomethane.

The Menshutkin reaction<sup>28,29</sup> is an important methyl transfer reaction and plays an essential role in many fields of chemistry ranging from biochemical processes (histone methylation,<sup>30</sup> methyltransferases<sup>31,32</sup>) to chemical synthesis.<sup>33</sup> Methyl-transfer reactions in biological systems are catalyzed by methyltransferases for which the most prominent enzymatic cofactor is *S*-adenosyl-L-methionine (SAM).<sup>31</sup> SAM is derived from ATP by the enzyme methionine synthase<sup>34</sup> and serves as a regulator of a variety of processes including DNA, tRNA, and rRNA methylation as well as immune response.<sup>35</sup> DNA methylation is governed by DNA methyltransferase (DNMTs) enzymes such as DNMT1, DNMT3A, and DNMT3B.<sup>36</sup> More recent findings suggest that DNA and histone methylation cooperate to maintain the cellular epigenomic landscape.<sup>37</sup> Finally, histone methylation has been found to be undone by

histone demethylases.<sup>38</sup>

Common examples of methylation reactions that have been studied extensively in the past are  $S_N2$  reactions<sup>23,39-47</sup> such as  $\text{Cl}^- + \text{MeBr} \rightarrow \text{MeCl} + \text{Br}^-$ <sup>26</sup> or  $\text{F}^- + \text{MeI} \rightarrow \text{MeF} + \text{I}^-$ <sup>46</sup> and the Menshutkin reaction.<sup>25,48-54</sup> The  $S_N2$  and Menshutkin reactions are of particular interest because of their importance in chemical synthesis.<sup>55</sup> The main difference between a standard  $S_N2$  reaction and a Menshutkin reaction is that for an  $S_N2$  reaction the reactant state is charged whereas it is neutral for a Menshutkin reaction, e.g.  $\text{NH}_3 + \text{NH}_2\text{-C}_6\text{H}_4\text{-Br} \rightarrow \text{NH}_2\text{-C}_6\text{H}_4\text{-NH}_3^+ + \text{Br}^-$  or  $\text{Pyr} + \text{MeCl} \rightarrow [\text{Pyr-Me}]^+ + \text{Cl}^-$ .<sup>52,54</sup> The Menshutkin reaction proceeds via a dipolar transition state (TS) to an ionic product and the TS is stabilized in polar solvents.<sup>50,54</sup>

The Menshutkin reaction is also a characteristic example for studying the effect of solvation on reactions<sup>53</sup> since it displays pronounced solvent effects on activation barriers.<sup>54,56,57</sup> Experimental studies have shown a decrease in the activation energy depending on the polarity of the solvent. The experimentally reported activation barrier for  $\text{Pyr} + \text{MeBr}$  in methanol is 22.5 kcal/mol which is 3.1 and 5.1 kcal/mol lower compared with apolar cyclohexane and di-n-butyl ether.<sup>54</sup> Further, an almost linear relationship between the natural log of the rate constants and polarity/polarizability of the solvents for the alkylation (Menshutkin) reaction between 1-bromodecane and 1,2-dimethylimidazol was observed.<sup>58</sup> DMSO was found to be the best solvent for accelerating the rate of heteroatom alkylations. Although solvent effects are evidently relevant for the Menshutkin reaction, surprisingly little is known about the molecular details of the reaction itself and the solvent ordering in particular.

Solvent effects for the  $\text{NH}_3 + \text{MeCl}$  and  $\text{Pyr} + \text{MeBr}$  reactions were previously considered with quantum mechanical (QM) and semi-empirical methods. For  $\text{NH}_3 + \text{MeCl}$  previous electronic structure calculations at the  $\text{HF}/6\text{-31++G}^*$ <sup>59</sup> and  $\text{B3PW91}/6\text{-31+G}^*$ <sup>60</sup> levels with

implicit polarizable continuum model (PCM) models<sup>61</sup> as well as QM/MM simulations at the B3LYP/MM level were carried out.<sup>62</sup> Also, both reactions were investigated with multi-scale reaction density functional theory (RxDFT) in acetonitrile.<sup>63</sup>

The present work addresses the question of how the presence and the nature of the solvent affects the reaction barrier height for two methyl transfer reactions  $\text{NH}_3 + \text{MeCl}$  and  $\text{Pyr} + \text{MeBr}$  (see Figure 1). For a comprehensive sampling of the molecular dynamics along the progression coordinate the multi state adiabatic reactive molecular dynamics (MS-ARMD) framework was used which provides a computational means to investigate chemical reactions (bond breaking/bond formation) with an efficiency comparable to an empirical force field.<sup>64</sup> Both, the energetics of the reaction and the organization of the solvent for critical points along the progression coordinate is analyzed. First, the force fields and their parametrization is described. This is followed by free energy calculations and the analysis of the catalytic effect, the organization of the solvent around the transition state and the solvent energetics. Finally, the results are discussed in a broader context.

## 2 Computational Methods

### 2.1 Molecular Dynamics Simulations

All molecular dynamics (MD) simulations were performed with CHARMM<sup>65</sup> with provision for forming and breaking bonds via MS-ARMD.<sup>64</sup> MD simulations were started following 500 steps of steepest descent and 500 steps of Adopted Basis Newton-Raphson minimization. Then, 500 ps of  $NpT$  dynamics were carried out using the leapfrog Verlet integrator<sup>66</sup> ( $\Delta t = 1$  fs) and a Hoover barostat<sup>67</sup> with a collision rate of  $5 \text{ ps}^{-1}$ . The  $NpT$  dynamics were followed by 2 ns ( $\Delta t = 1$  fs) of free dynamics in the  $NVT$  ensemble using SHAKE.<sup>68</sup> Periodic Boundary Conditions (PBC) together with the Particle Mesh Ewald (PME<sup>69</sup>) method were



used for the long range electrostatic interaction. The cut-off for non-bonded, switching, and smoothing was 16 Å, 14 Å, and 12 Å, respectively.

The simulations in the different solvents were started by solvating the reactant states of the two reactions,  $\text{NH}_3 + \text{MeCl}$  and  $\text{Pyr} + \text{MeBr}$ , in pre-equilibrated, cubic solvent boxes. Due to the different shapes and sizes of the solvents, cubic box sizes were chosen accordingly. They were of length  $L = 30$  Å (water),  $L = 25$  Å (methanol),  $L = 28$  Å (acetonitrile),  $L = 27$  Å (benzene), and  $L = 30$  Å (cyclohexane), respectively.

## 2.2 Parametrization of the Force Field

All electronic structure calculations of reactant, transition, and product states were performed with Gaussian09<sup>70</sup> at the MP2/6-311++G(2d,2p) level of theory. For simulating Me-transfer between a donor and an acceptor a reactive force field to break and form chemical bonds is required. MS-ARMD is a reactive molecular dynamics implementation which combines individually weighted connectivities, describing different states by parametrized force fields. So called, GAPOs (GAussian  $\times$  POLynomials) for describing the adiabatic barrier are added to smoothly connect reactant and product side to form the global reactive Potential Energy Surface (PES). GAPOs are calculated from the energy difference  $\Delta V_{ij}(x)$  ( $= V_j(x) - V_i(x)$ ) between two states  $i$  and  $j$ .

For the Menshutkin reactions  $\text{NH}_3 + \text{MeCl}$  and  $\text{Pyr} + \text{MeBr}$  the parametrization of the reactant and product states started with optimization of the reactant and product geometries at the MP2/6-311++G(2d,2p) level of theory. Initial force fields for the reactant and product molecules ( $\text{NH}_3$ ,  $\text{MeCl}$ , methylammonium cation, pyridine, and methyl pyridine cation, respectively), were obtained from Swissparam.<sup>71</sup> The initial Mulliken charges for the fit were those from the electronic structure calculations.

For  $\text{NH}_3 + \text{MeCl}$  the reference reactant complex structures were generated from a 1 ns gas-phase MD simulation in the *NVT* ensemble using the Swissparam parametrization. In the MD simulations the distance between the ammonia and chloromethane was kept close to the equilibrium distance in the reactant state using a harmonic constraint. From this trajectory 1000 structures were stored for which reference energies at the MP2/6-311++G(2d,2p) level were determined. For the  $\text{Pyr} + \text{MeBr}$  reaction a similar procedure was followed. The reference reactant complex structures were generated from a 1 ns gas-phase MD simulation in the *NVT* ensemble using the Swissparam parametrization. The distance between the pyridine and bromomethane was kept close to the equilibrium distance in the reactant state using a harmonic constraint. From this trajectory 1700 structures were stored for which reference energies at the MP2/6-311++G(2d,2p) level were determined.

In addition to the conformational ensemble of the reactant states, structures and energies along the internal reaction coordinate (IRC) path were used together with product state geometries which were generated from scanning along the C–Cl and C–Br distances, respectively. As the main focus in the present work is on the energetics involving the reactant, TS, and ion-pair states, no full parametrization for the ionic products  $[\text{H}_3\text{NMe}]^+$  and  $[\text{PyrMe}]^+$  was carried out. This would be required if the reaction is followed out and beyond the solvent-separated ion pairs which is not done in the following. Hence, on the product side the relaxed scan only involved C–Cl separations between 2.5 Å to 6 Å and C–Br distances ranging from 3 Å to 13 Å, respectively. Subsequently all force field parameters were fitted to the reference energies<sup>19,72–74</sup> by using a downhill simplex algorithm.<sup>75</sup> Finally, the reactant and product force fields were connected by fitting the GAPOs along the IRC using a genetic algorithm. The bond, angle, dihedral and van der Waals parameters of the force field are provided in Tables S1 and S2. Further, the resulting fit of the Menshutkin reactions for  $\text{NH}_3 + \text{MeCl}$  and  $\text{Pyr} + \text{MeBr}$  contains three Gaussians and the GAPO parameters are pro-

vided in Tables S3 and S4.

## 2.3 Umbrella sampling

Since direct sampling of the two reactions is not possible due to the high reaction barriers ( $> 20$  kcal/mol), umbrella sampling (US)<sup>76</sup> simulations were used to follow the reaction path. The reaction coordinate chosen here was the difference between the carbon-X bond of the reactant and the carbon-N bond in the product, i.e.  $r_c = d_{CX} - d_{CN}$  where X = Cl, Br for the  $\text{NH}_3 + \text{MeCl}$  and  $\text{Pyr} + \text{MeBr}$  reactions, respectively. Simulations were carried out for equidistant windows between  $r_c = -1.3$  and  $1.6$  Å with  $\Delta r_c = 0.1$  Å and with  $k_{\text{umb}} = 150$  kcal/mol/rad<sup>2</sup>.

US simulations for both systems were performed in a sequential manner, i.e. restarting a new US simulation from the structure and velocities of the previous simulation. Each window was simulated for 50 ps and window statistics was accumulated after equilibration for 5 ps. Statistics from all the windows were combined to yield the 1-dimensional potential of mean force (PMF) using the Weighted Histogram Analysis Method (WHAM)<sup>77,78</sup> with a tolerance of 0.001.

## 2.4 Solvent Distribution

To characterize the solvent distribution and change along the reaction pathway, separate 2 ns MD simulations for  $\text{NH}_3 + \text{MeCl}$  and  $\text{Pyr} + \text{MeBr}$  in the  $NVT$  ensemble were carried out. The reactant, TS and product state structures were constrained at their MP2/6-311++G(2d,2p) optimized geometries and the center of mass (CoM) of the solute was at the center of the simulation box. To analyze the solvent distributions the solute was reoriented and superimposed to minimize the structural root mean squared deviation. For the  $\text{NH}_3 + \text{MeCl}$  reaction

first the methyl-carbon was translated to the origin of the box, then the ammonia-N was aligned along the  $x$ -axis and one of the three hydrogens bonded to the ammonia-N was placed into the  $xy$ -plane. For the Pyr+MeBr reaction the pyridine-N was translated to the origin of the box, the methyl-C was then aligned along the  $x$ -axis and one of the hydrogens bonded to the ammonia-N was placed in the  $xy$ -plane.

From the 2000 snapshots the water-oxygen ( $O_W$ ), methanol-oxygen ( $O_{MeOH}$ ) and acetonitrile-nitrogen ( $N_{ACN}$ ) coordinates were extracted whereas for benzene and cyclohexane the center of mass was determined and used for further analysis. The CoM was chosen for apolar solvents because selecting one specific atom as for the polar solvents is less meaningful as this would lead to skewing the results due to rotation of the solvent molecule. Based on these reference coordinates, all solvent molecules with the point of reference ( $O_W$ ,  $O_{MeOH}$ ,  $N_{ACN}$ , and the CoMs of benzene and hexane) within  $-1 \leq z \leq +1$  Å were selected and further analyzed to give a 2-dimensional solvent distribution. The collected data points were then smoothed with a 2D bivariate normal kernel density estimation.<sup>79,80</sup> Solvent boxes were divided into 100 bins along the  $x$ - and  $y$ -axes to generate a  $100 \times 100$  grid. Then, the solvent density around each of the grid points was smoothed using a 2D Gaussian distribution with a width of 1.5 Å. Isocontours were drawn at 90%, 75%, 50%, 25%, and 10% of the highest occupation for each solvent to allow direct comparison.

## 3 Results and Discussion

### 3.1 The Potential Energy Surfaces

The correlation between the fitted force field and the MP2 reference energies is reported in Figure 2. As the main interest of the present work is the forward process, i.e.  $NH_3 + MeCl \rightarrow [H_3NMe]^+ + Cl^-$  and  $Pyr + MeBr \rightarrow [PyrMe]^+ + Br^-$ , the parametrization was focused on the

reactant state including the transition state region. For the 1000 and 1700 reference reactant state structures the RMSDs are 0.78 kcal/mol and 0.93 kcal/mol, respectively, for the two reactions. As the inset demonstrates, the minimum energy path (MEP) is well reproduced by these parametrizations, too. Such a quality is comparable with that found in previous studies. The reactive PES for the hydrogen abstraction reaction between  $\text{MgO}^+$  and ethane had a RMSD of 1.5 kcal/mol with respect to MP2/aug-cc-pVTZ for the reactant and 1.1 kcal/mol for the product state.<sup>81</sup> For the Diels-Alder reaction between 2,3-dibromobutadiene and maleic anhydride had a RMSD of 2.9 kcal/mol for the overall reaction.<sup>82</sup> For the product side (ion-pair) the RMSDs along the C-Cl and C-Br separations are 3.60 kcal/mol and 2.41 kcal/mol for the two reactions, respectively, and dominated by high energy structures for long C-Cl<sup>-</sup> separations.

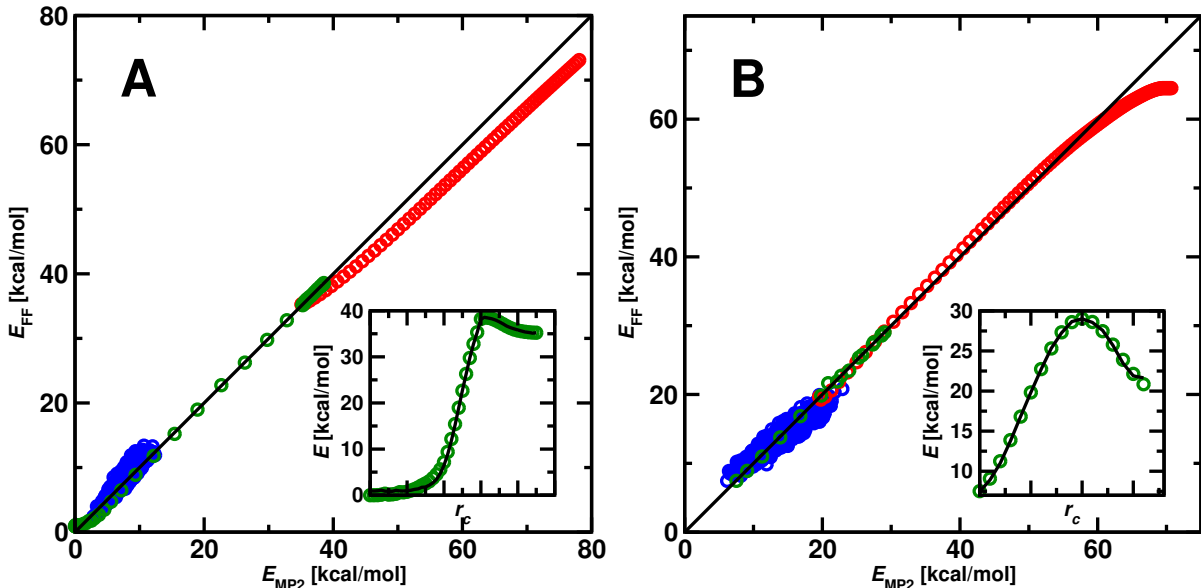


Figure 2: Panel A: Menshutkin reaction of ammonia with chloromethane to methylammonium chloride: Energy correlation between the fitted force field and the MP2 reference for 1000 reactant structures (blue, RMSD of 0.78 kcal/mol) and 70 product structures (red, RMSD of 3.60 kcal/mol). Panel B: Menshutkin reaction of pyridine with bromomethane to methyl pyridine and  $\text{Br}^-$ : Energy correlation between the fitted force field and the MP2 reference for 1700 reactant structures (blue, RMSD=0.93 kcal/mol) and 101 product structures (red, RMSD=2.41 kcal/mol). The two insets show the IRC points (green circles) together with the energies from the reactive force field (black line) based on the GAPO-fits to connect the reactant and product force fields.

### 3.2 Umbrella Sampling Simulations and Potentials of Mean Force

*NH<sub>3</sub>+MeCl*: The 1-dimensional PMFs for the NH<sub>3</sub>+MeCl reaction are reported in Figure 3 and Table 1 summarizes the activation free barriers. Umbrella sampling simulations based on the parametrized, reactive force field for the NH<sub>3</sub>+MeCl reaction yields a free energy barrier  $\Delta G^\ddagger = 35.8$  kcal/mol in the gas-phase. This compares with an activation barrier of 38.5 kcal/mol from the IRC in the gas-phase at the MP2/6-311++G(2d,2p) level. Previous electronic structure calculations for the same reaction reported barrier heights of 36.2 kcal/mol and 32.7 kcal/mol at the HF/6-31++G\*<sup>59</sup> and B3PW91/6-31+G\*<sup>60</sup> levels, respectively.

Table 1: Free energy barrier for the Menshutkin reaction of NH<sub>3</sub>+MeCl (in kcal/mol) calculated with MS-ARMD and US in different solvents (Sim.). The experimental (Exp.)  $\Delta G^\ddagger$  value is for the NH<sub>3</sub> + MeI reaction in water (0.05 M MeI)<sup>83</sup> and in methanol (0.1 M MeI).<sup>84</sup> Hexane = cyclohexane.

	Gas	Water	Methanol	Acetonitrile	Benzene	Hexane
Sim.	35.8	18.0 $\pm$ 0.5	20.5	20.6	24.1	33.9 $\pm$ 1.4
Exp.		23.5 <sup>83</sup>	20.8 <sup>84</sup>			
Literature	36.2 <sup>59</sup> / 32.7 <sup>60</sup>	16.1 <sup>59</sup> / 21.7 <sup>54</sup> / 25.6 <sup>85</sup> / 15.7 $\pm$ 0.3 <sup>62</sup> / 21.9 $\pm$ 2.7 <sup>62</sup>		16.8 <sup>63</sup> / 22.3 <sup>63</sup>		32.6 <sup>54</sup>

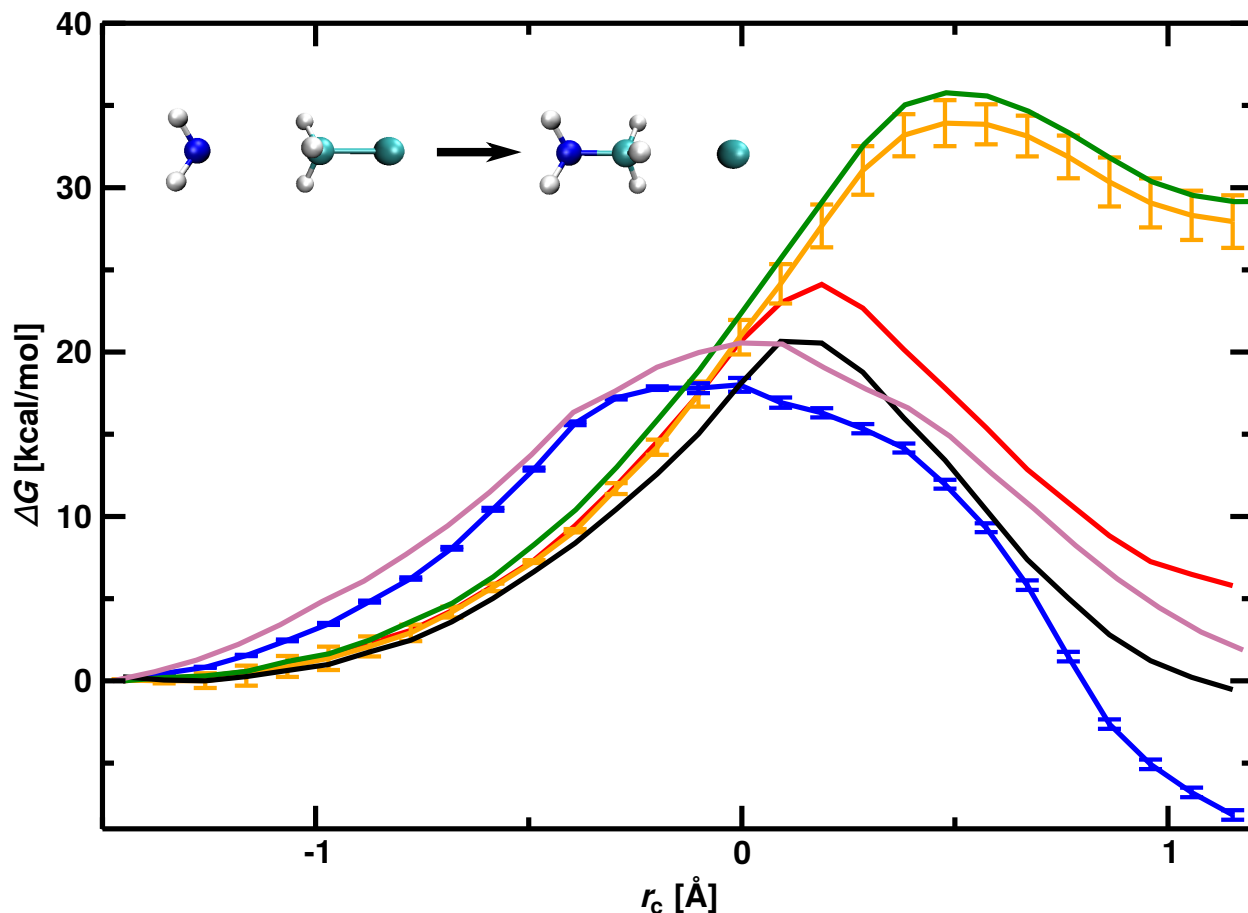


Figure 3: Potentials of mean force for the Menshutkin reaction for  $\text{NH}_3 + \text{MeCl}$  in water (blue), methanol (purple), benzene (red), acetonitrile (black), and cyclohexane (orange) from umbrella sampling simulations. For comparison, the PMF from US in the gas phase is also reported in green.

In water, methanol, acetonitrile, benzene, and cyclohexane the barrier heights from the 1-dimensional PMFs are  $18.0 \pm 0.5$ , 20.5, 20.6, 24.1, and  $33.9 \pm 1.4$  kcal/mol, respectively. Representative error bars were determined from bootstrapping for polar (water) and apolar (cyclohexane) solvent. For the simulations in water and methanol, the activation energies of  $18.0 \pm 0.5$  and 20.6 kcal/mol compare with the experimentally reported values of 23.5<sup>83</sup> and 20.8 kcal/mol<sup>84</sup> for  $\text{NH}_3 + \text{MeI}$ , respectively. Only qualitative comparison between experiment and simulations is possible because a) results from experiments are only available for MeI and not MeBr, and b) the MeI concentration was 0.05 M in water and 0.1

M in methanol.<sup>83</sup> Previously, the minimum energy pathway for the  $\text{NH}_3 + \text{MeCl}$  reaction in explicit water was determined at the HF/6-31G\* level of theory, followed by single-point energy calculations at the MP4SDTQ/6-31+G\* level. The resulting activation barrier was 25.6 kcal/mol.<sup>85</sup> In a more recent study the barrier heights from a semi-empirical QM study were  $15.7 \pm 0.3$  and  $21.9 \pm 2.7$  kcal/mol, respectively.<sup>62</sup> The activation barrier was  $15.7 \pm 0.3$  kcal/mol when directly computed from the lower level PM3/MM calculations and increased to  $21.9 \pm 2.7$  kcal/mol by using a higher level, indirect B3LYP/MM methodology. In this method, configurational sampling and iterative pathway optimization were carried out with a lower-level PM3/MM Hamiltonian, and analyzed with WHAM to obtain the lower-level reaction free energy profile. This was followed by thermodynamic perturbation<sup>86</sup> to a higher level target B3LYP/MM Hamiltonian with 6-31G\* basis set to obtain a corrected free energy profile.<sup>62</sup>

As expected, polar solvents show a stronger effect in reducing the reaction barrier height compared to apolar solvents, see Figure 3. All polar solvents and benzene find an earlier TS compared to vacuum for which it is at  $r_c = 0.5$  Å. For benzene, acetonitrile, methanol and water the TS progressively shifts towards the reactant with  $r_c$  ranging from  $r_c = 0.2$  Å to  $r_c = -0.1$  Å. Furthermore, the free energy profile widens considerably when going from the gas phase to methanol and water as a solvent and compared with acetonitrile and the apolar solvents. Water and methanol are the smallest and most polar solvents and are able to approach and interact with the solute more directly than the larger and apolar solvent molecules which leads to widening of the PMF. For benzene the packing is easier due to its planar structure compared to the chair conformation of cyclohexane. Further, benzene has stronger electrostatic interactions with the solute as a result of negatively charged carbon atoms. Thus, benzene displays a barrier reduction closer to the polar water solvent than the apolar cyclohexane.



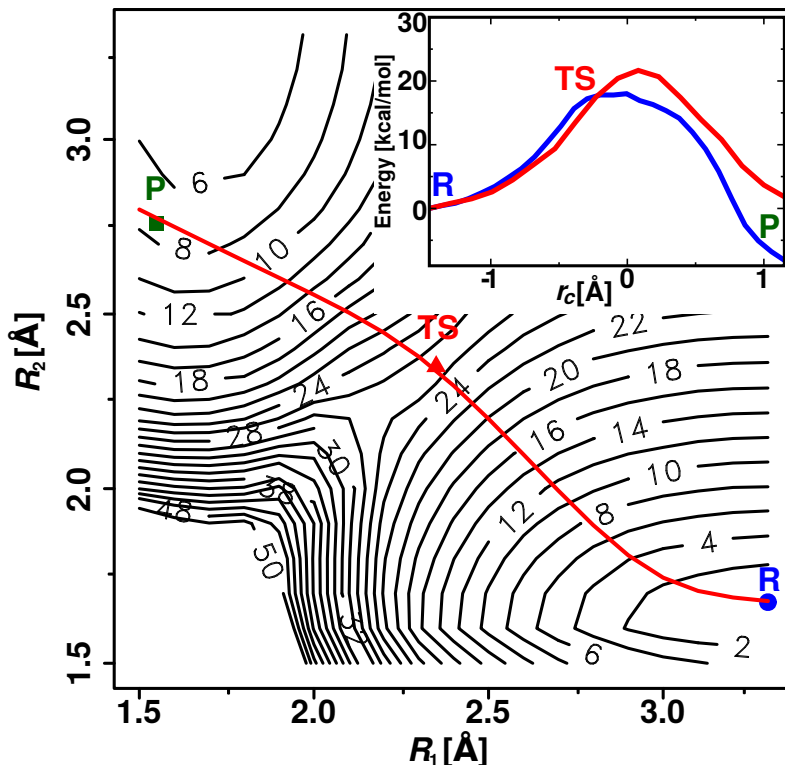


Figure 4: 2D PMF of  $\text{NH}_3+\text{MeCl}$  in water, scanned through reaction coordinates of  $R_1 = d_{\text{C-N}}$  and  $R_2 = d_{\text{C-Cl}}$ . Relative positions of reactant (blue circle), transition state (red triangle) and product (green square) shown on the plot. The red line denotes the minimum energy pathway from reactant to product (see text). Contours are drawn in increments of 2 kcal/mol. The inset shows the 1D PMF extracted from the 2D surface (red line) superimposed onto the 1D PMF (blue line) of  $\text{NH}_3+\text{MeCl}$  in water from Figure 3.

In order to assess how representative the 1-dimensional PMFs are, a 2-dimensional PMF surface was determined for  $\text{NH}_3+\text{MeCl}$  in water, see Figure 4. The two reaction coordinates  $R_1$  and  $R_2$  were the distance between the methyl-C and ammonia-N atom ( $R_1 = d_{\text{C-N}}$ ) and between the methyl-C and the Cl atoms ( $R_2 = d_{\text{C-Cl}}$ ), respectively. In the simulations,  $R_1$  and  $R_2$  were constrained by a harmonic potential with a force constant of 1000 kcal/mol and the N-C-Cl angle was constrained to remain linear. For a fixed  $R_1$  value the 2D PMF was scanned along the  $R_2$  coordinate and statistics accumulated from 50 ps sampling for each value of the reaction coordinate. From this, the 2d PMF was constructed using 2D-

WHAM<sup>77,78</sup> with a tolerance of 0.001.

A direct comparison between the 1D PMF from the US (blue) and the minimum energy path on the 2D PMF (red) is shown in the inset of Figure 4. The minimum energy path on the 2D PMF was calculated by fixing  $R_2$  values on a grid with  $\Delta R_2 = 0.1 \text{ \AA}$  and minimizing along  $R_1$ . This provides a realistic path between reactant and TS. Between TS and the product the true MEP is slightly different which is, however, of lesser interest in the present work. The activation barrier calculated from the 2D PMF is 21.7 kcal/mol which is 3.7 kcal/mol higher than that of the 1D PMF (see Figure 4 inset) and closer to the experimentally determined activation barrier of 23.5 kcal/mol for the  $\text{NH}_3 + \text{MeI}$  reaction. The fact that the 1D and 2D PMF are quite close to one another supports the results of the 1D PMFs reported for the other solvents.<sup>83</sup> Part of the difference in the barrier heights between the 1D and 2D PMFs can be attributed to the constraints that were used in computing the 2D PMF. On the other hand, the 2D PMF yields additional insights into mechanistic aspects of the reaction. The PES clarifies that the Menshutkin reaction is concerted from the perspective of the two reaction coordinates. As  $R_1$  contracts from the reactant (R) to the product (P),  $R_2$  elongates. The transition region is comparatively steep along the transition pathway but flat orthogonal to it. For separations  $R_1$  and  $R_2$  smaller than 2.2  $\text{\AA}$  a strong repulsion is found.

*Pyr+MeBr:* The 1-dimensional PMFs for the Pyr+MeBr Menshutkin reaction are reported in Figure 5 and Table 2 summarizes the activation free barriers. In the gas phase US yields an activation free energy of  $\Delta G^\ddagger = 29.7 \text{ kcal/mol}$  compared with the barrier height of 29.0 kcal/mol from the IRC at the MP2/6-311++G(2d,2p) level of theory. In water, methanol, and acetonitrile the computed barriers are 17.9, 22.1, and 23.2 kcal/mol and in apolar solvents they are 22.2 and 28.1 kcal/mol for benzene and hexane, respectively. Experimentally reported barrier heights as determined from the measured rates for acetonitrile and hex-

ane were 22.5 and 27.6 kcal/mol, respectively,<sup>54</sup> and the ordering and absolute values agree favourably with the present simulations.

Table 2: Free energy barrier for the Menshutkin reaction of Pyr+MeBr (in kcal/mol) calculated with MS-ARMD and US in different solvents (Sim.). The experimental (Exp.) values for  $\Delta G^\ddagger$  are from Ref.<sup>54</sup> for Pyr+MeBr. Hexane = cyclohexane.

	Gas	Water	Methanol	Acetonitrile	Benzene	Hexane
Sim.	29.7	17.9	22.1	23.2	22.2	28.1
Exp. <sup>54</sup>				22.5		27.6

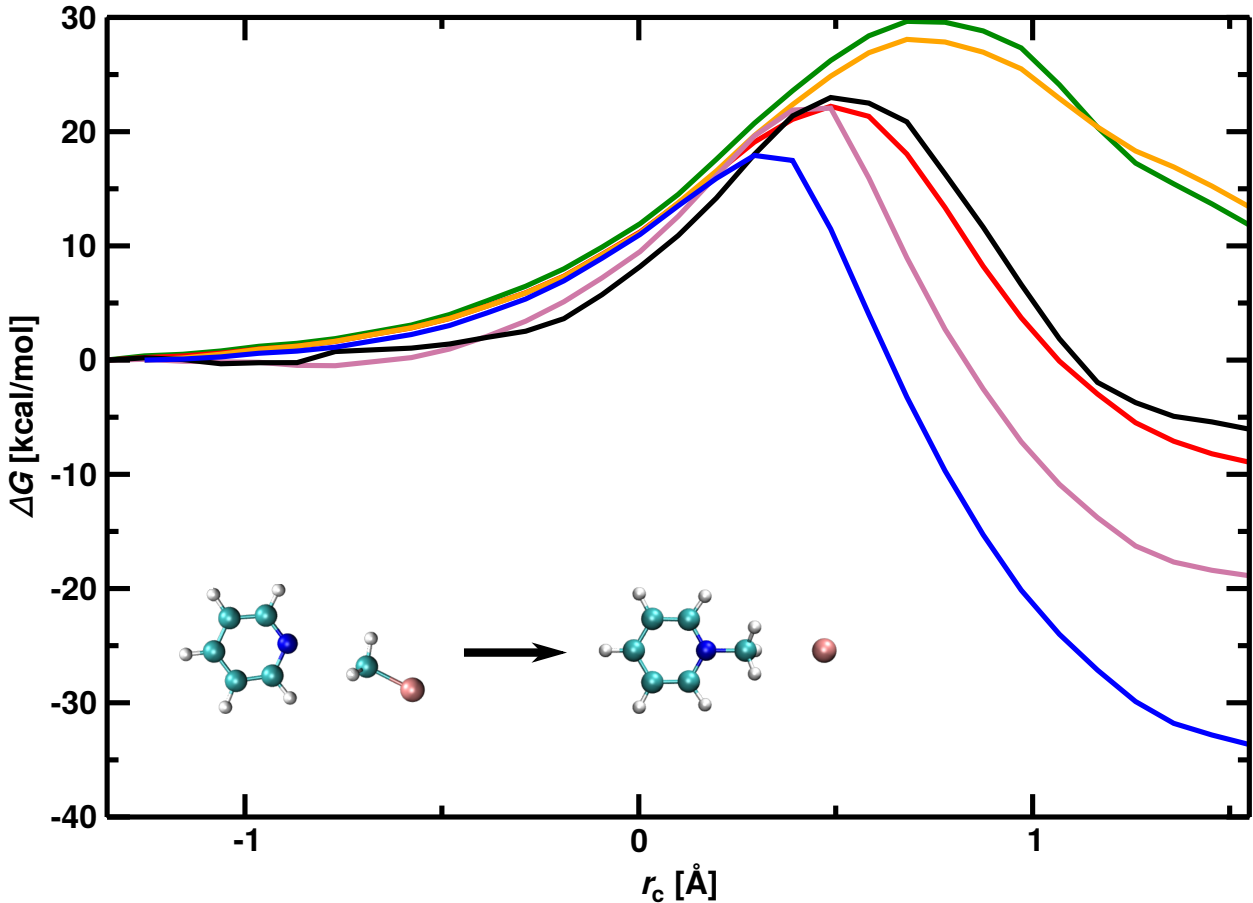


Figure 5: Potentials of mean force for the Menshutkin reaction for Pyr+MeBr in water (blue), methanol (purple), acetonitrile (black), benzene (red), and cyclohexane (orange). For comparison, the result from US in the gas phase is reported in green.

For polar solvents the reaction barrier height decreases with increasing polarity of the sol-

vent. Notably, for the reaction in benzene, the barrier height of 22.2 kcal/mol is close to that for methanol and lower than that for acetonitrile. The catalytic effect of benzene has been observed previously from computations for the Menshutkin reaction of  $\text{NH}_3 + \text{NH}_2\text{-C}_6\text{H}_4\text{-Br} \rightarrow \text{NH}_2\text{-C}_6\text{H}_4\text{-NH}_3^+ + \text{Br}^-$  at the MP2/6-31+G(d) level.<sup>52</sup> In this case, the gas-phase activation barrier of 33.2 kcal/mol decreased to 22.8 kcal/mol in benzene.

The position of the TS in the different solvents is directly correlated with the catalytic effect. Cyclohexane, which displays a lower barrier to that in the gas phase has the TS at  $r_c \sim 0.7 \text{ \AA}$ , whereas solvents with catalytic effect shift the TS to progressively shorter values of  $r_c$ . Benzene, which reduces the barrier height slightly more strongly than methanol, has a TS at around  $r_c = 0.5 \text{ \AA}$  which is also the value for methanol. In water, which shows the strongest reduction in the barrier, the maximum of the PMF is shifted towards an even smaller value of  $r_c = 0.3 \text{ \AA}$ . This difference in catalytic strength and shift in TS position can be explained by the stabilizing effects of the three polar solvents water, methanol and acetonitrile. The aromatic benzene, even though apolar, achieves a similar stabilization due to its planar structure and electrostatics.

### 3.3 Solvent Distributions

The MD simulations also offer the opportunity to analyze the solvent distribution along the reaction at molecular resolution. For this, separate simulations were carried out for the reactant, product, and transition states of both reactions in all solvents. The solute was constrained at the optimized geometries of the reactant, TS, and ion-pair structures from the MP2/6-311G++(2d,2p) calculations and the solvent was sampled from unbiased simulations.

For the  $\text{NH}_3 + \text{MeCl}$  reaction the solvent distribution around the solute in polar (water, methanol, acetonitrile) and apolar (benzene and hexane) solvent is presented in Figures 6

and 7, respectively. In general, for polar solvents the distribution around the reactant and the TS differs. This is most evident for acetonitrile and methanol (Figure 6 top and middle) but also for water (Figures 6 bottom). Solvent density maxima around the  $\text{Cl}^-$  anion in the TS were found for methanol, water, and acetonitrile. The asymmetry around  $\text{Cl}^-$  anion is partly due to the thin analysis slab ( $-1\text{\AA} < z < 1\text{\AA}$ ) which was necessary to avoid congestion of the solvent distribution for other parts of the molecule. The solvent density maxima are explained by the favourable interaction of the OH-hydrogen atoms (water and methanol) or the positively charged carbon atom (acetonitrile) with the  $\text{Cl}^-$  anion. For the TS in methanol and water there are three density maxima around the H-atoms of ammonia, which are potential H-bonding sites. For the reactants, the density maximum is around  $\text{Cl}^-$  in polar solvents. For all three structures, the innermost isocontour is closest to the solute for water as solvent as packing is tightest due to its small size.

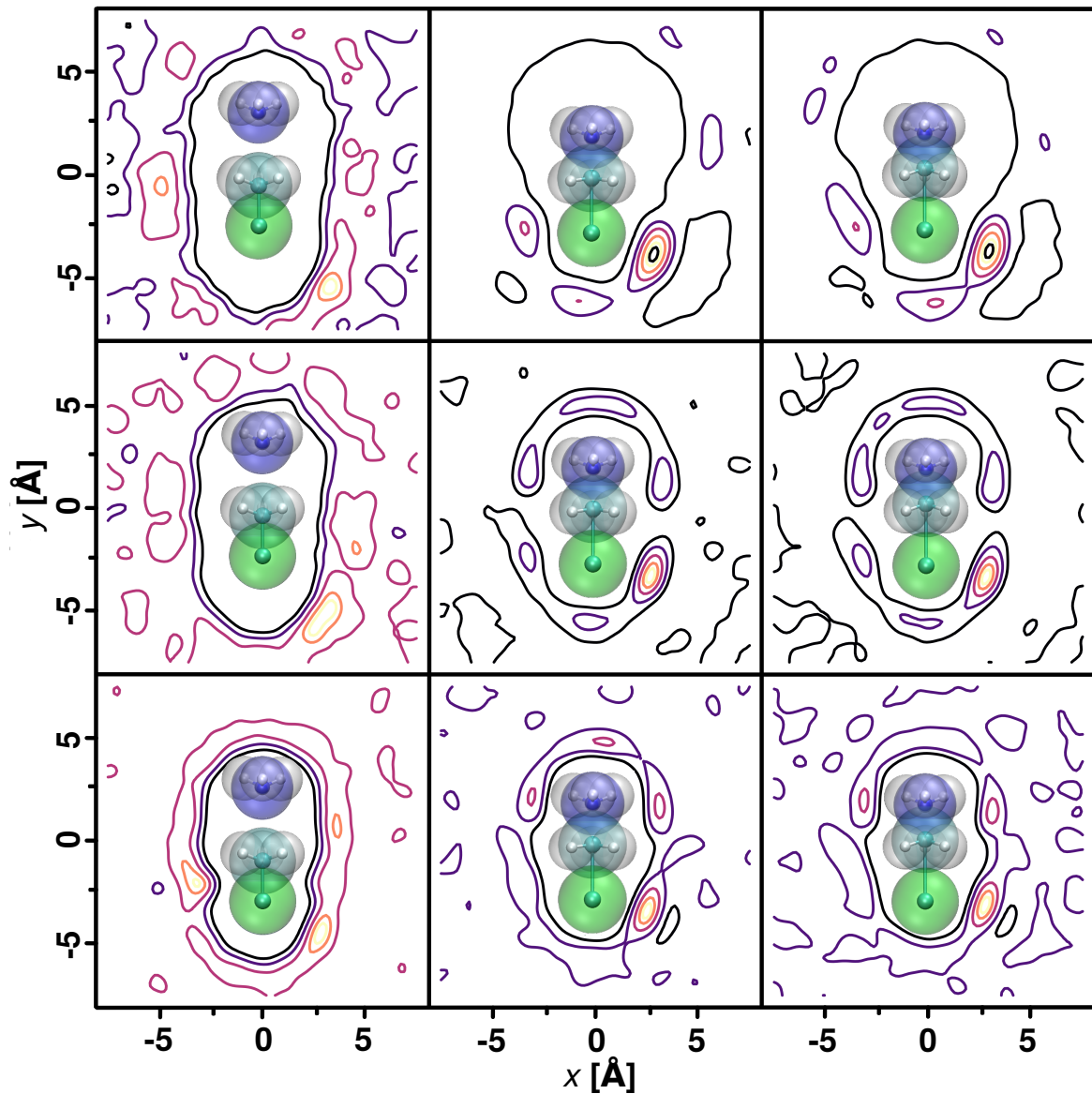


Figure 6: 2-dimensional solvent distributions for  $\text{NH}_3+\text{MeCl}$  from 2 ns simulations in polar solvents: acetonitrile, methanol and water (from top to bottom) around the reactant, TS, and product state structures of the solute (from left to right) projected onto the  $xy$ -plane containing the chloride, carbon and nitrogen atoms. Units in Å. In the simulations and the figure the solute is in its optimized structure for the reactant, TS, and product state, respectively, at the MP2/6-311++G(2d,2p) level of theory. The color code for atoms is H (white), C (cyan), N (blue) and Cl (green). Note the larger solvent rearrangement between reactant and TS compared with TS and product structures.

Solvent structures for the TS and the product state are comparable. This can, in part, be ra-

tionalized by the similarity of the TS and ion-pair structures of the solute and the differences between the reactant and TS structures: the N-C distances for the Cl-Me-NH<sub>3</sub> arrangement are 3.30 Å, 1.81 Å, and 1.55 Å for the reactant, TS, and ion-pair in vacuum, respectively. Similarly, the C-Cl distances are 1.80 Å, 2.42 Å, and 2.76 Å for reactant, TS and ion-pair. This similarity between the TS and ion-pair structure is reminiscent of a manifestation of the Hammond postulate which states that if two states occur consecutively along a reaction and have nearly the same energy content, their interconversion will involve only a small reorganization of the molecular structures. For the solute structures this is evidently the case as the TS and the contact-ion-pair structures only differ little. Similarly, the solvent distributions between reactant and TS differ, in general, considerably more compared with the change in solvent structure between TS and the product.

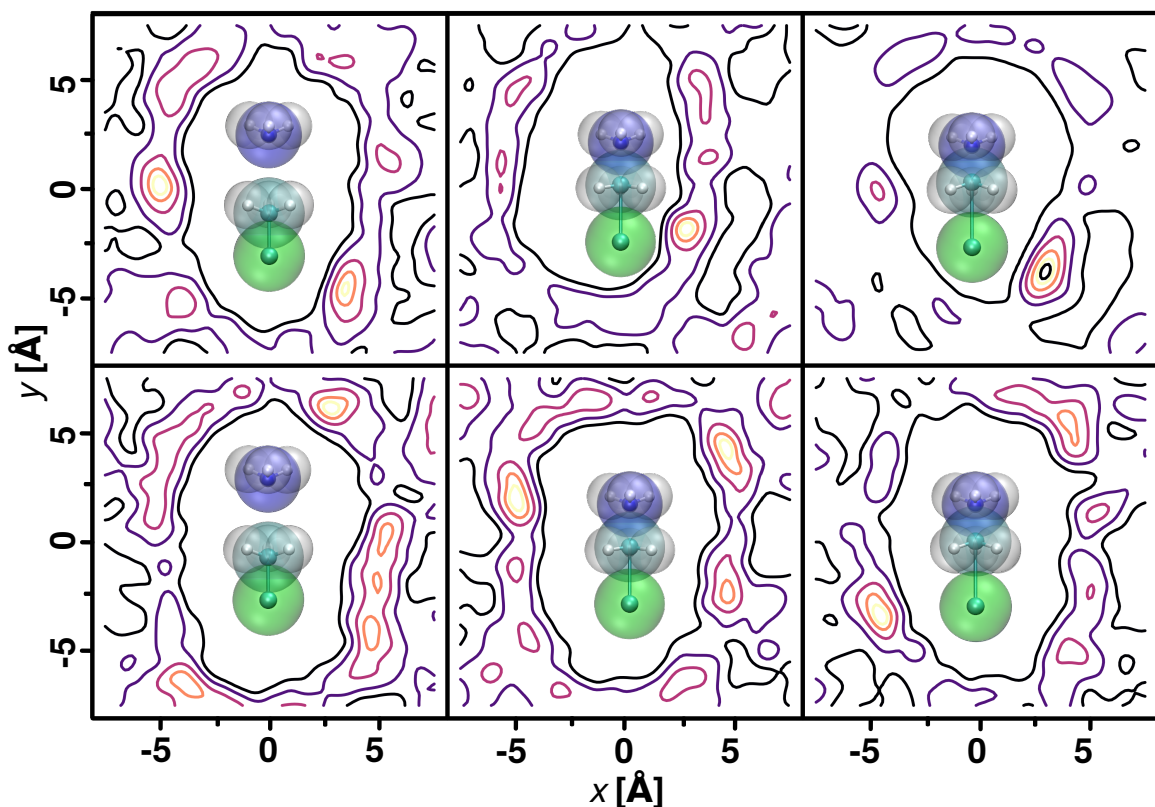


Figure 7: 2-dimensional solvent distributions for  $\text{NH}_3+\text{MeCl}$  in apolar solvents: benzene (top) and hexane (bottom) around the reactant, TS, and product state structures of the solute (from left to right) projected onto the  $xy$ -plane containing the chloride, carbon and nitrogen atoms. Units in Å. In the simulations and the figure the solute is in its optimized structure for the reactant, TS, and product state, respectively, at the MP2/6-311++G(2d,2p) level of theory. The color code for atoms is H (white), C (cyan), N (blue) and Cl (green).

For the apolar solvents, the distribution around the solute showed less pronounced maxima, see Figure 7, except for the product state in benzene. For cyclohexane the solvent distribution is considerably less structured than for the polar solvents which indicates the weak interaction between solute and solvent in this case and is the underlying reason for the limited catalytic effect of cyclohexane for the  $\text{NH}_3+\text{MeCl}$  reaction. Contrary to cyclohexane, the density maximum of solvent molecules around the  $\text{Cl}^-$  anion for the product in benzene, and to some degree for the TS, were present. The packing around the solute was more dense in benzene, especially at the TS.



For the Pyr+MeBr reaction the solvent distribution around the solute in polar and apolar solvents is presented in Figures S1 and S2, respectively. Similar to the  $\text{NH}_3+\text{MeCl}$  reaction, the solvent distribution around the reactant and the TS differed. For the reactant the  $\text{N}_{\text{Pyr}}\text{-C-Br}$  angle deviates from linearity whereas in the TS and for the contact-ion-pair it was linear. Due to the positively charged pyridine-H atoms multiple density maxima around the ring were observed for all states in polar solvents. In methanol, the solvent distribution was heterogeneous, with multiple density maxima around the solute and beyond the first solvation shell. Compared with acetonitrile, methanol is more tightly packed around the solute. Contrary to that, the solvent distribution for water was comparatively homogeneous. Although multiple density maxima for water near the solute are observed for the first solvation shell, the solvent distribution becomes more homogeneous beyond the first solvation shell for all three states of the solute. For the contact-ion-pair solvent structuring occurs for water and methanol, but not for acetonitrile.

For apolar solvents, see Figure S2, the solvent distribution around the solute was less dense compared to the polar solvents. The maxima around the positively charged hydrogen atoms appear for benzene. However, the densities around the  $\text{Br}^-$  anion were less pronounced than for polar solvents. The packing around the  $\text{Br}^-$  anion was tighter for the TS and contact-ion-pair compared with the reactant state. Cyclohexane packs more densely around the solute for Pyr+MeBr compared to  $\text{NH}_3+\text{MeCl}$ . This can be explained by the larger size of the solute, which allows the bulkier, apolar solvent to accommodate better, than around a smaller solute. The trend of similar solvent distribution around TS and product is also found for these two solvents.

### 3.4 Solvent Energetics

The simulations also provide quantitative information about the relative solvent-solvent interactions along the reaction pathway with respect to an arbitrary reference state which is the reactant in the following. Two different analyses were carried out for the energetics of solvent molecules as a function of the reaction coordinate. First, the energetics of the solvent molecules within the first solvation shell, i.e. molecules in direct contact with the solute, were investigated as a function of the reaction coordinate from the umbrella sampling simulations. Secondly, a similar analysis was carried out from 2 ns simulations with the solute frozen in the reactant, TS, and contact-ion-pair geometries at the MP2/6-311G++(2d,2p) level of theory for a) the first solvation shell and b) for the entire simulation box.

For the first analysis only solvent molecules within a cutoff distance of 5 Å of any atom of the solute were retained which corresponds approximately to the first solvation shell for each solvent. For each of the umbrellas from the US simulations the average solvent-solvent interaction energy per solvent molecule was determined together with the fluctuation around the mean for the  $\text{NH}_3 + \text{MeCl}$  reaction in water (see Figure 8) and for the  $\text{Pyr} + \text{MeBr}$  reaction in methanol (see Figure S3).

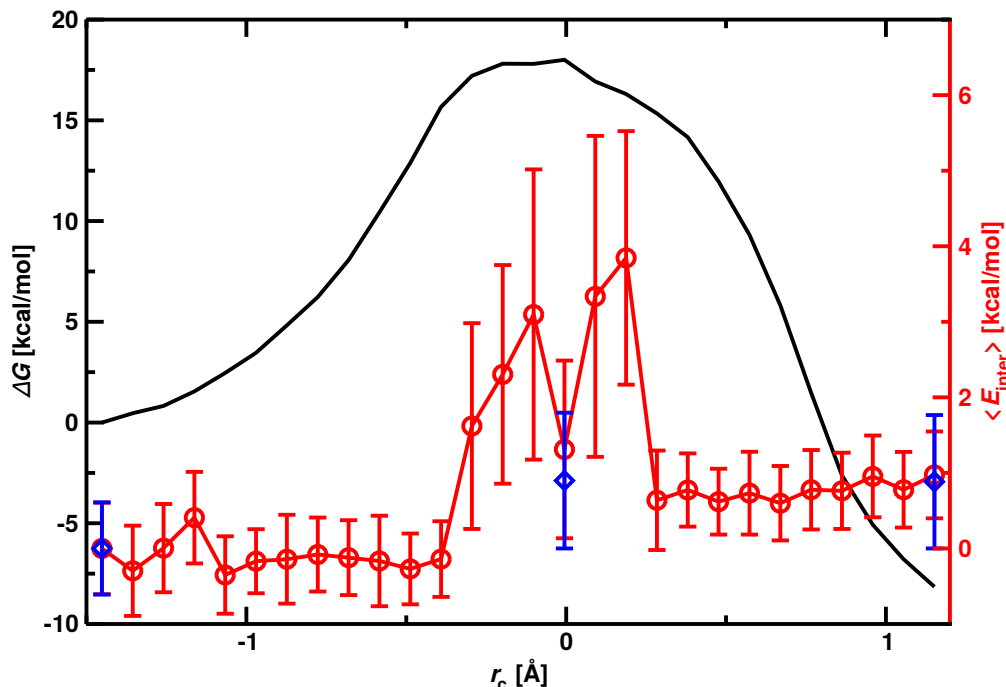


Figure 8: Potentials of mean force for the Menshutkin reaction for  $\text{NH}_3 + \text{MeCl}$  in water (black line) and the energy of solvent molecules within 5 Å of the solute in kcal/mol/molecule (red line). The circles are the mean for a given umbrella together with the standard deviation from the mean as a bar. The blue diamonds are the average solvent interaction energies from the 2 ns simulations with the frozen solute (reactant, TS and contact-ion-pair) structures together with the standard deviation from the mean as a bar.

The average energy per solvent molecule with respect to the reactant within 5 Å (red trace) superimposed on the PMF of  $\text{NH}_3 + \text{MeCl}$  in water (black) is shown in Figure 8. Starting from the reactant structure at  $r_c = -1.2$  Å the average interaction energy remains around  $\sim -0.5$  kcal/mol/molecule up to  $r_c \sim -0.4$  Å after which it suddenly increases. Before the transition state the average interaction energy per water molecule is destabilized by  $\sim 2.5$  kcal/mol to accommodate the transition state of the solute. At the transition state,  $r_c = 0$ , the solvent is destabilized with respect to the reactant by about 1 kcal/mol per water molecule (but stabilized relative to the structures before the TS by about 1.5 kcal/mol). Beyond the TS the surrounding water molecules arrange again in a more unfavourable conformation before their average interaction energies return to levels comparable to that of the reactant of around  $\sim 0.8$  kcal/mol at  $r_c \sim 0.3$  Å. This demonstrates that the water solvent

participates actively in the reaction progress.

For the Pyr+MeBr reaction in methanol the average energy per solvent molecule with respect to the reactant within 5 Å is shown in Figure S3. Starting from the reactant structure the average energy per solvent molecule remains at  $\sim -1$  kcal/mol/molecule up to  $r_c \sim -0.8$  Å. Upon approaching the transition state ( $r_c \sim -0.5$  Å) the average interaction energy between the solvent molecules increases (destabilization). Compared with the NH<sub>3</sub>+MeCl reaction in water the destabilization of the solvent starts earlier, though. Before reaching the TS at  $r_c \sim 0.4$  Å the average interaction energy decreases and reaches a value similar to that of the reactant albeit with larger variance. Between the TS and the product structure the interaction energy increases again and then drops back to levels of the reactant structure. Since the TS and product states are structurally similar to each other (see Figure S1 and its discussion), the effects on the average solvent energetics are less prominent in the later stage of the reaction.

The 2D-solvent distributions for  $r_c = [-0.3, -0.2, -0.1]$  Å are shown in Figure S4. It is found that the density maxima around MeBr decrease in amplitude as the reaction proceeds from reactant towards TS, especially for the region between the methyl-H and the Pyr-H. The protic nature of methanol promotes H-bonding which results in density maxima around the region between the methyl-H and the Pyr-H. As the isocontours are drawn at the same heights in all representations, the populations are directly comparable. It is found that as the system approaches the region with  $r_c = -0.2$  Å from either the reactant or the TS side, the ordering decreases appreciably thus, correlated motions of solvent molecules are required in this region of the reaction profile. This partly explains in a “time lapse” picture why reactions “take more time” (ps and longer) than the actual reactive step (which is rather fs). which is reflected in the energetic destabilization of the solvent at this position relative to the reactant or TS structure. Hence, changes in the solvent distribution are directly reflected

in the average solvent-solvent energetics.

Again, the more extended 2 ns *NVT* simulations with the solute frozen in its reactant, TS, and product state geometry were analyzed and the average interaction energies for solvent molecules within 5 Å of the solute were determined, see Tables 3 and 4, and the blue diamonds in Figure S3. These results compare favourably with the analysis of the US simulations and indicate that the sampling from the US simulations is representative.

Table 3: Solvent-solvent interaction for  $\text{NH}_3+\text{MeCl}$  for solvent molecules within 5 Å of any of the solute atoms. The average energy per solvent molecule of TS and product states with respect to the reactant, in kcal/mol. The standard deviation from the mean per solvent molecule given in parentheses. Water-45 labels the simulations in the 45 Å water box.

Solvent	Reactant	TS	Product
Water	0 (0.06)	0.06 (0.06)	0.08 (0.06)
Water-45	0 (0.93)	0.07 (1.05)	0.09 (1.04)
Methanol	0 (0.65)	0.30 (0.41)	0.41 (0.32)
Acetonitrile	0 (0.28)	0.02 (0.28)	0.10 (0.27)
Benzene	0 (2.03)	0.67 (6.30)	0.49 (2.34)
Cyclohexane	0 (1.87)	0.21 (2.26)	0.24 (2.22)

In addition, one simulation for the  $\text{NH}_3+\text{MeCl}$  reaction in a 45 Å cubic box (Water-45 in Table 3) was carried out to assess the influence of the box size on the solvent energetics. With an increased number of water molecules the fluctuation in the solvent interaction energies increases for the first solvation shell. When analyzing the average interaction energies and fluctuations around the mean for all water molecules for the two box sizes the differences were found to be insignificant. Hence, the box size for the simulations appears to influence the structural dynamics of the water molecules closest to the solute. This is an effect worth to be explored but outside the scope of the present work.<sup>87</sup> For the solvent-solvent energies a more general observation is also that with the reactant state as the zero of energy, the average energy content of the solvent for the TS and contact-ion pair structures is generally

higher.

Table 4: Solvent-solvent interaction for Pyr+MeBr for solvent molecules within 5 Å of any of the solute atoms. The average total energy of solvent boxes of TS and product per solvent molecule with respect to the reactant, in kcal/mol. The standard deviation from the mean per solvent molecule given in parentheses.

Solvent	Reactant	TS	Product
Water	0 (0.23)	0.61 (0.53)	0.62 (0.55)
Methanol	0 (0.13)	0.40 (0.39)	0.38 (0.40)
Acetonitrile	0 (1.10)	2.13 (1.16)	2.18 (1.20)
Benzene	0 (3.88)	0.65 (4.71)	0.70 (4.64)
Cyclohexane	0 (1.84)	0.19 (2.15)	0.25 (2.23)

## 4 Conclusion

The energetics and solvent distributions for two Menshutkin reactions are quantitatively characterized and analyzed at molecular detail. Barrier height reductions in going from the gas phase to more polar solvents are consistent with what is known from experiments. The solvent distributions change appreciably between reactant, transition state, and product states. These changes in solvent structure are also reflected in the average solvent-solvent interactions. One notable feature of the solvent-solvent interactions is the fact that the fluctuation around the mean increases considerably when going from small to larger solvent molecules.

Starting from the reactant structure the average solvent-solvent interaction within the first solvation shell ( $\sim 5$  Å within the solute) remains small and constant up to about 50 % of the barrier height after which it increases rapidly (see Figures 8 and S3). Around the transition state the solvent-solvent strain relaxes, increases again and then returns to levels slightly higher than that of the reactant state. This points towards an intimate interplay between

solute and solvent degrees of freedom along the reaction coordinate. It is also of interest to note that the fluctuations around the mean increase appreciably around the TS. Analysis of the solvent distributions also suggests that in approaching the TS collective motions of the solvent molecules are required. This may be one of the reasons why time scales for reactions can differ dramatically from the actual time to cross the barrier. It will be of interest to compare these findings with those from unbiased simulations. However, to obtain sufficient statistics a large number of reactive trajectories will be required, and ideally a system with a lower activation barrier is considered.

In summary, a computationally tractable and qualitatively correct description - as compared with the few experimental data available - of the Menshutkin reaction the gas phase and in various solvents has been presented. Analysis of the solvent degrees of freedom point towards tight coupling between solute and solvent dynamics with increased fluctuations in the solvent-solvent interactions around the transition state. The necessary solvent reorganization between reactant and TS structures of the solvent requires extensive sampling which is reflected in the time scale separation between the true rate of a reaction in solution and the time required to traverse the barrier.

## Data Availability

Data sets are available from the corresponding author upon reasonable request.

## Supporting Information

The Supporting Information contains Tables S1 to S4 for the parametrization of the force fields and additional Figures S1 to S4.

## 5 Acknowledgments

The authors gratefully acknowledge financial support from the Swiss National Science Foundation through grant 200021-117810 and to the NCCR-MUST.

## References

- (1) Warshel, A.; Weiss, R. M. An Empirical Valence Bond Approach for Comparing Reactions in Solutions and in Enzymes. *J. Am. Chem. Soc.* **1980**, *102*, 6218–6226.
- (2) Yadav, A.; Jackson, R. M.; Holbrook, J. J.; Warshel, A. Role of Solvent Reorganization Energies in the Catalytic Activity of Enzymes. *J. Am. Chem. Soc.* **1991**, *113*, 4800–4805.
- (3) Luzhkov, V.; Warshel, A. Microscopic Calculations of Solvent Effects on Absorption Spectra of Conjugated Molecules. *J. Am. Chem. Soc.* **1991**, *113*, 4491–4499.
- (4) Zhan, S.; Mårtensson, D.; Purg, M.; Kamerlin, S. C.; Ahlquist, M. S. Capturing the Role of Explicit Solvent in the Dimerization of Ru<sup>V</sup>(bda) Water Oxidation Catalysts. *Angew. Chemie - Int. Ed.* **2017**, *56*, 6962–6965.
- (5) Kamerlin, S. C.; Haranczyk, M.; Warshel, A. Are Mixed Explicit/Implicit Solvation Models Reliable for Studying Phosphate Hydrolysis? A Comparative Study of Continuum, Explicit and Mixed Solvation Models. *ChemPhysChem* **2009**, *10*, 1125–1134.
- (6) Ranaghan, K. E.; Ridder, L.; Szeftczyk, B.; Sokalski, W. A.; Hermann, J. C.; Mulholland, A. J. Transition State Stabilization and Substrate Strain in Enzyme Catalysis: ab initio QM/MM Modelling of the Chorismate Mutase Reaction. *Org. Biomol. Chem.* **2004**, *2*, 968–980.



- (7) Shaw, K. E.; Woods, C. J.; Mulholland, A. J. Compatibility of Quantum Chemical Methods and Empirical (MM) Water Models in Quantum Mechanics/Molecular Mechanics Liquid Water Simulations. *J. Phys. Chem. Lett.* **2010**, *1*, 219–223.
- (8) Carlsson, J.; Åqvist, J. Calculations of Solute and Solvent Entropies from Molecular Dynamics Simulations. *Phys. Chem. Chem. Phys.* **2006**, *8*, 5385–5395.
- (9) Bingemann, D.; King, A. M.; Crim, F. F. Transient Electronic Absorption of Vibrationally Excited CH<sub>2</sub>I<sub>2</sub>: Watching Energy Flow in Solution. *J. Chem. Phys.* **2000**, *113*, 5018–5025.
- (10) Almlöf, M.; Carlsson, J.; Åqvist, J. Improving the Accuracy of the Linear Interaction Energy Method for Solvation Free Energies. *J. Chem. Theory Comput.* **2007**, *3*, 2162–2175.
- (11) Elles, C. G.; Cox, M. J.; Crim, F. F. Vibrational Relaxation of CH<sub>3</sub>I in the Gas Phase and in Solution. *J. Chem. Phys.* **2004**, *120*, 6973–6979.
- (12) Preston, T. J.; Shaloski, M. A.; Crim, F. F. Probing the Photoisomerization of CHBr<sub>3</sub> and CHI<sub>3</sub> in Solution with Transient Vibrational and Electronic Spectroscopy. *J. Phys. Chem. A* **2013**, *117*, 2899–2907.
- (13) Rivera, C. A.; Winter, N.; Harper, R. V.; Benjamin, I.; Bradforth, S. E. The Dynamical Role of Solvent on the ICN Photodissociation Reaction: Connecting Experimental Observables Directly with Molecular Dynamics Simulations. *Phys. Chem. Chem. Phys.* **2011**, *13*, 8269–8283.
- (14) Orr-Ewing, A. J. Perspective: Bimolecular Chemical Reaction Dynamics in Liquids. *J. Chem. Phys.* **2014**, *140*, 090901.
- (15) Claeysens, F.; Ranaghan, K. E.; Lawan, N.; Macrae, S. J.; Manby, F. R.; Harvey, J. N.; Mulholland, A. J. Analysis of Chorismate Mutase Catalysis by QM/MM Modelling of

- Enzyme-Catalysed and Uncatalysed Reactions. *Org. Biomol. Chem.* **2011**, *9*, 1578–1590.
- (16) Severance, D. L.; Jorgensen, W. L. Effects of Hydration on the Claisen Rearrangement of Allyl Vinyl Ether from Computer Simulations. *J. Am. Chem. Soc.* **1992**, *114*, 10966–10968.
- (17) Guest, J. M.; Craw, J. S.; Vincent, M. A.; Hillier, I. H. The Effect of Water on the Claisen Rearrangement of Allyl Vinyl Ether: Theoretical Methods Including Explicit Solvent and Electron Correlation. *Perkin Trans. 2* **1997**, 71–74.
- (18) Cramer, C. J.; Truhlar, D. G. What Causes Aqueous Acceleration of the Claisen Rearrangement? *J. Am. Chem. Soc.* **1992**, *114*, 8794–8799.
- (19) Brickel, S.; Meuwly, M. Molecular Determinants for Rate Acceleration in the Claisen Rearrangement Reaction. *J. Phys. Chem. B* **2019**, *123*, 448–456.
- (20) Hwang, J. K.; King, G.; Creighton, S.; Warshel, A. Simulation of Free Energy Relationships and Dynamics of  $S_N2$  Reactions in Aqueous Solution. *J. Am. Chem. Soc.* **1988**, *110*, 5297–5311.
- (21) Shaik, S. The Collage of  $S_N2$  Reactivity Patterns: A State Correlation Diagram Model. *Prog. Phys. Org. Chem.* **1985**, *15*, 197–337.
- (22) Chandrasekhar, J.; Smith, S. F.; Jorgensen, W. L. Theoretical Examination of the  $S_N2$  Reaction Involving Chloride Ion and Methyl Chloride in the Gas Phase and Aqueous Solution. *J. Am. Chem. Soc.* **1985**, *107*, 154–163.
- (23) Merkel, A.; Zahradník, R.; Havlas, Z. Evaluation of the Rate Constant for the  $S_N2$  Reaction  $\text{CH}_3\text{F} + \text{H}^- \rightarrow \text{CH}_4 + \text{F}^-$  in the Gas Phase. *J. Am. Chem. Soc.* **1988**, *110*, 8355–8359.

- (24) Gao, J.; Xia, X. A Two-Dimensional Energy Surface for a type II  $S_N2$  Reaction in Aqueous Solution. *J. Am. Chem. Soc.* **1993**, *115*, 9667–9675.
- (25) Fradera, X.; Amat, L.; Torrent, M.; Mestres, J.; Constans, P.; Besald, E.; Marti, J.; Simon, S.; Lobato, M.; Oliva, J. M. et al. Analysis of the Changes on the Potential Energy Surface of Menshutkin Reactions Induced by External Perturbations. *J. Mol. Struct.* **1996**, *371*, 171–183.
- (26) Adamovic, I.; Gordon, M. S. Solvent Effects on the  $S_N2$  Reaction: Application of the Density Functional Theory-Based Effective Fragment Potential Method. *J. Phys. Chem. A* **2005**, *109*, 1629–1636.
- (27) Shaik, S.; Ioffe, A.; Reddy, A. C.; Pross, A. Is the Avoided Crossing State a Good Approximation for the Transition State of a Chemical Reaction? An Analysis of Menshutkin and Ionic  $S_N2$  Reactions. *J. Am. Chem. Soc.* **2006**, *116*, 262–273.
- (28) Menshutkin, N. Beiträge zur Kenntnis der Affinitätskoeffizienten der Alkylhaloide und der Organischen Amine. *Zeitschrift für Phys. Chemie* **1890**, *5*, 589–600.
- (29) Menshutkin, N. Über die Affinitätskoeffizienten der Alkylhaloide und der Amine. *Zeitschrift für Phys. Chemie* **1890**, *6*, 41–57.
- (30) Allfrey, V. G.; Faulkner, R.; Mirsky, A. Acetylation and Methylation of Histones and Their Possible Role in the Regulation of RNA Synthesis. *Proc. Nat. Acad. Sci. USA* **1964**, *51*, 786.
- (31) Schubert, H. L.; Blumenthal, R. M.; Cheng, X. Many Paths to Methyltransfer: A Chronicle of Convergence. *Trends Biochem. Sci.* **2003**, *28*, 329–335.
- (32) Schmidt, T.; Schwede, T.; Meuwly, M. Computational Analysis of Methyl Transfer Reactions in Dengue Virus Methyltransferase. *J. Phys. Chem. B* **2014**, *118*, 5882–5890.

- (33) Arava, S.; Diesendruck, C. E. Strategies for the Synthesis of N-Arylammonium Salts. *Synthesis* **2017**, *49*, 3535–3545.
- (34) Ding, W.; Smulan, L. J.; Hou, N. S.; Taubert, S.; Watts, J. L.; Walker, A. K. S-Adenosylmethionine Levels Govern Innate Immunity Through Distinct Methylation-Dependent Pathways. *Cell Metab.* **2015**, *22*, 633–645.
- (35) Scavetta, R. D.; Thomas, C. B.; Walsh, M. A.; Szegedi, S.; Joachimiak, A.; Gumpert, R. I.; Churchill, M. E. Structure of Rsr I Methyltransferase, a Member of the N 6-adenine  $\beta$  Class of DNA Methyltransferases. *Nucleic Acids Res.* **2000**, *28*, 3950–3961.
- (36) Tajima, S.; Suetake, I.; Takeshita, K.; Nakagawa, A.; Kimura, H. Domain Structure of the Dnmt1, Dnmt3a, and Dnmt3b DNA Methyltransferases. *DNA Methyltransferases-Role and Function* **2016**, 63–86.
- (37) Li, Y.; Chen, X.; Lu, C. The Interplay Between DNA and Histone Methylation: Molecular Mechanisms and Disease Implications. *EMBO Rep.* **2021**, e51803.
- (38) Shi, Y.; Lan, F.; Matson, C.; Mulligan, P.; Whetstine, J. R.; Cole, P. A.; Casero, R. A.; Shi, Y. Histone Demethylation Mediated by the Nuclear Amine Oxidase Homolog LSD1. *Cell* **2004**, *119*, 941–953.
- (39) Lieder, C. A.; Brauman, J. I. A Technique for Detection of Neutral Products in Gas-Phase, Ion-Molecule Reactions. *Int. J. Mass Spectrom. Ion Phys.* **1975**, *16*, 307–319.
- (40) Olmstead, W. N.; Brauman, J. I. Gas-Phase Nucleophilic Displacement Reactions. *J. Am. Chem. Soc.* **1977**, *99*, 4219–4228.
- (41) Hierl, P. M.; Ahrens, A. F.; Henchman, M.; Viggiano, A. A.; Paulson, J. F. Rate Constants and Product Distributions as Functions of Temperature for the Reaction of  $\text{OH}^-(\text{H}_2\text{O})_{0,1,2}$  with  $\text{CH}_3\text{CN}$ . *Int. J. Mass Spectrom. Ion Process.* **1987**, *81*, 101–122.

- (42) Barlow, S. E.; Van Doren, J. M.; Bierbaum, V. M. The Gas-Phase Displacement Reaction of Chloride Ion with Methyl Chloride as a Function of Kinetic Energy. *J. Am. Chem. Soc.* **1988**, *110*, 7240–7242.
- (43) Vande Linde, S. R.; Hase, W. L. A Direct Mechanism for  $S_N2$  Nucleophilic Substitution Enhanced by Mode Selective Vibrational Excitation. *J. Am. Chem. Soc.* **1989**, *111*, 2349–2351.
- (44) DePuy, C. H.; Gronert, S.; Mullin, A.; Bierbaum, V. M. Gas-Phase  $S_N2$  and E2 Reactions of Alkyl Halides. *J. Am. Chem. Soc.* **1990**, *112*, 8650–8655.
- (45) Kato, S.; Davico, G. E.; Lee, H. S.; DePuy, C. H.; Bierbaum, V. M. Deuterium Kinetic Isotope Effects in Gas Phase  $S_N2$  Reactions. *Int. J. Mass Spectrom.* **2001**, *210-211*, 223–229.
- (46) Stei, M.; Carrascosa, E.; Kainz, M. A.; Kelkar, A. H.; Meyer, J.; Szabó, I.; Czakó, G.; Wester, R. Influence of the Leaving Group on the Dynamics of a Gas-Phase  $S_N2$  Reaction. *Nat. Chem.* **2016**, *8*, 151–156.
- (47) Carrascosa, E.; Meyer, J.; Zhang, J.; Stei, M.; Michaelsen, T.; Hase, W. L.; Yang, L.; Wester, R. Imaging Dynamic Fingerprints of Competing E2 and  $S_N2$  Reactions. *Nat. Commun.* **2017**, *8*, 1–7.
- (48) Viers, J. W.; Schug, J. C.; Stovall, M. D.; Seeman, J. I. MNDO Study of Reaction Pathways for  $S_N2$  Reactions. Menshutkin Reaction Potential Energy Surfaces. *J. Comp. Chem.* **1984**, *5*, 598–605.
- (49) Amovilli, C.; Mennucci, B.; Floris, F. M. MCSCF Study of the  $S_N2$  Menshutkin Reaction in Aqueous Solution within the Polarizable Continuum Model. *J. Phys. Chem. B* **1998**, *102*, 3023–3028.

- (50) Castejon, H.; Wiberg, K. B.; Sklenak, S.; Hinz, W. Solvent Effects on Methyl Transfer Reactions. 2. The Reaction of Amines with Trimethylsulfonium Salts. *J. Am. Chem. Soc.* **2001**, *123*, 6092–6097.
- (51) Sola, M.; Lledos, A.; Duran, M.; Bertran, J.; Abboud, J. L. M. Analysis of Solvent Effects on the Menshutkin Reaction. *J. Am. Chem. Soc.* **1991**, *113*, 2873–2879.
- (52) Jiang, L.; Orimoto, Y.; Aoki, Y. Substituent Effects on Menshutkin-Type Reactions in the Gas Phase and Solutions: Theoretical Approach from the Orbital Interaction View. *J. Chem. Theory Comput.* **2013**, *9*, 4035–4045.
- (53) Acevedo, O.; Jorgensen, W. L. Exploring Solvent Effects Upon the Menshutkin Reaction Using a Polarizable Force Field. *J. Phys. Chem. B* **2010**, *114*, 8425–8430.
- (54) Castejon, H.; Wiberg, K. B. Solvent Effects on Methyl Transfer Reactions. 1. The Menshutkin Reaction. *J. Am. Chem. Soc.* **1999**, *121*, 2139–2146.
- (55) Gronet, S.; DePuy, C. H.; Bierbaum, V. M. Deuterium Isotope Effects in Gas-Phase Reactions of Alkyl Halides: Distinguishing E2 and S<sub>N</sub>2 Pathways. *J. Am. Chem. Soc.* **1991**, *113*, 4009–4010.
- (56) Auriel, M.; de Hoffmann, E. Quantitative Study of Solvent Effects on the Menshutkin Reaction Between 1, 4-diazabicyclo [2.2.2] octane and 2-chloroethylbenzene, 2-bromoethylbenzene, and 2-iodoethylbenzene. Part 2. Mixed Solvents. *J. Chem. Soc., Perkin trans. 2* **1979**, 325–329.
- (57) Maran, U.; Pakkanen, T. A.; Karelson, M. Semiempirical Study of the Solvent Effect on the Menshutkin Reaction. *J. Chem. Soc., Perkin trans. 2* **1994**, 2445–2452.
- (58) Komarova, A. O.; Dick, G. R.; Luterbacher, J. S. Diformylxylose as a New Polar Aprotic Solvent Produced from Renewable Biomass. *Green Chem.* **2021**, *23*, 4790–4799.

- (59) Poater, J.; Solà, M.; Duran, M.; Fradera, X. Effects of Solvation on the Pairing of Electrons in a Series of Simple Molecules and in the Menshutkin Reaction. *J. Phys. Chem. A* **2001**, *105*, 6249–6257.
- (60) Halls, M. D.; Schlegel, H. B. Chemistry Inside Carbon Nanotubes: the Menshutkin  $S_N2$  Reaction. *J. Phys. Chem. B* **2002**, *106*, 1921–1925.
- (61) Miertuš, S.; Scrocco, E.; Tomasi, J. Electrostatic Interaction of a Solute with a Continuum. A Direct Utilizaion of *ab initio* Molecular Potentials for the Prevision of Solvent Effects. *Chem. Phys.* **1981**, *55*, 117–129.
- (62) Pan, X.; Li, P.; Ho, J.; Pu, J.; Mei, Y.; Shao, Y. Accelerated Computation of Free Energy Profile at *ab initio* Quantum Mechanical/Molecular Mechanical Accuracy via a Semi-Empirical Reference Potential. II. Recalibrating Semi-Empirical Parameters with Force Matching. *Phys. Chem. Chem. Phys.* **2019**, *21*, 20595–20605.
- (63) Tang, W.; Zhao, J.; Jiang, P.; Xu, X.; Zhao, S.; Tong, Z. Solvent Effects on the Symmetric and Asymmetric  $S_N2$  Reactions in the Acetonitrile Solution: A Reaction Density Functional Theory Study. *J. Phys. Chem. B* **2020**, *124*, 3114–3122.
- (64) Nagy, T.; Reyes, J. Y.; Meuwly, M. Multisurface Adiabatic Reactive Molecular Dynamics. *J. Chem. Theory. Comput.* **2014**, *10*, 1366–1375.
- (65) Brooks, B. R.; Brooks, C. L., III; Mackerell, A. D., Jr.; Nilsson, L.; Petrella, R. J.; Roux, B.; Won, Y.; Archontis, G.; Bartels, C.; Boresch, S. et al. CHARMM: The Biomolecular Simulation Program. *J. Chem. Comp.* **2009**, *30*, 1545–1614.
- (66) Verlet, L. Computer Experiments on Classical Fluids. I. Thermodynamical Properties of Lennard-Jones Molecules. *Phys. Rev.* **1967**, *159*, 98–103.
- (67) Hoover, W. G. Canonical Dynamics: Equilibrium Phase-Space Distributions. *Phys. Rev. A* **1985**, *31*, 1695–1697.

- (68) VanGunsteren, W.; Berendsen, H. Algorithms for Macromolecular Dynamics and Constraint Dynamics. *Mol. Phys.* **1977**, *34*, 1311–1327.
- (69) Essmann, U.; Perera, L.; Darden, M. L. B.; Lee, H.; Pedersen, L. G.; Essmann, U.; Perera, L.; Berkowitz, M. L.; Darden, T.; Lee, H. et al. A Smooth Particle Mesh Ewald Method. *J. Chem. Phys.* **1995**, *103*, 8577–8593.
- (70) Frisch, M. J.; Trucks, G. W.; Schlegel, H. B.; Scuseria, G. E.; Robb, M. A.; Cheeseman, J. R.; Scalmani, G.; Barone, V.; Mennucci, B.; Petersson, G. A. et al. Gaussian09 Revision {D}.01.
- (71) Zoete, V.; Cuendet, M. A.; Grosdidier, A.; Michielin, O. SwissParam: A Fast Force Field Generation Tool for Small Organic Molecules. *J. Comput. Chem.* **2011**, *32*, 2959–2368.
- (72) Brickel, S.; Das, A.; Unke, O.; Turan, H.; Meuwly, M. Reactive Molecular Dynamics for the  $[\text{Cl}-\text{CH}_3-\text{Br}]^-$  Reaction in the Gas Phase and in Solution: A Comparative Study Using Empirical and Neural Network Force Fields. *Electron. Struct.* **2019**, *1*, 024002.
- (73) Brickel, S.; Meuwly, M. OH-Stretching Overtone Induced Dynamics in  $\text{HSO}_3\text{F}$  from Reactive Molecular Dynamics Simulations. *J. Phys. Chem. A* **2017**, *121*, 5079–5087.
- (74) Reyes, J. Y.; Brickel, S.; Unke, O. T.; Nagy, T.; Meuwly, M.  $\text{HSO}_3\text{Cl}$ : a Prototype Molecule for Studying OH-stretching Overtone Induced Photodissociation. *Phys. Chem. Chem. Phys.* **2016**, *18*, 6780–6788.
- (75) Nelder, J.; Mead, R. A Simplex Method for Function Minimization. *Chem. Phys.* **1965**, *7*, 308–313.
- (76) Kottalam, J.; Case, D. A. Dynamics of Ligand Escape from the Heme Pocket of Myoglobin. *J. Am. Chem. Soc.* **1988**, *110*, 7690–7697.



- (77) Kumar, S.; Rosenberg, J. M.; Bouzida, D.; Swendsen, R. H.; Kollman, P. A. The Weighted Histogram Analysis Method for Free-energy Calculations on Biomolecules. I. The Method. *J. Comput. Chem.* **1992**, *13*, 1011–1021.
- (78) Souaille, M.; Roux, B. Extension to the Weighted Histogram Analysis Method: Combining Umbrella Sampling with Free Energy Calculations. *Comput. Phys. Commun.* **2001**, *135*, 40–57.
- (79) Rosenblatt, M. Remarks on Some Nonparametric Estimates of a Density Function. *Ann. Math. Stat.* **1956**, *27*, 832–837.
- (80) Parzen, E. On Estimation of a Probability Density Function and Mode. *Ann. Math. Stat.* **1962**, *33*, 1065–1076.
- (81) Sweeny, B. C.; Pan, H.; Kassem, A.; Sawyer, J. C.; Ard, S. G.; Shuman, N. S.; Vigiano, A. A.; Brickel, S.; Unke, O. T.; Upadhyay, M. et al. Thermal Activation of Methane by  $\text{MgO}^+$ : Temperature Dependent Kinetics, Reactive Molecular Dynamics Simulations and Statistical Modeling. *Phys. Chem. Chem. Phys.* **2020**, *22*, 8913–8923.
- (82) Rivero, U.; Turan, H. T.; Meuwly, M.; Willitsch, S. Reactive Atomistic Simulations of Diels-Alder Type Reactions: Conformational and Dynamic Effects in the Polar Cycloaddition of 2, 3-dibromobutadiene Radical Ions with Maleic Anhydride. *Mol. Phys.* **2021**, *119*, e1825852.
- (83) Okamoto, K.; Fukui, S.; Shingu, H. Kinetic Studies of Bimolecular Nucleophilic Substitution. VI. Rates of the Menschkin Reaction of Methyl Iodide with Methylamines and Ammonia in Aqueous Solutions. *Bull. Chem. Soc. of Jpn* **1967**, *40*, 1920–1925.
- (84) Okamoto, K.; Fukui, S.; Nitta, I.; Shingu, H. Kinetic Studies of Bimolecular Nucleophilic Substitution. VIII. The Effect of Hydroxylic Solvents on the Nucleophilicity of Aliphatic Amines in the Menschutkin Reaction. *Bull. Chem. Soc. of Jpn* **1967**, *40*, 2354–2357.

- (85) Gao, J. A Priori Computation of a Solvent-Enhanced  $S_N2$  Reaction Profile in Water: the Menshutkin Reaction. *J. Am. Chem. Soc.* **1991**, *113*, 7796–7797.
- (86) Zwanzig, R. W. High-Temperature Equation of State by a Perturbation Method. I. Nonpolar Gases. *J. Chem. Phys.* **1954**, *22*, 1420–1426.
- (87) El Hage, K.; Hedin, F.; Gupta, P. K.; Meuwly, M.; Karplus, M. Valid molecular dynamics simulations of human hemoglobin require a surprisingly large box size. *Elife* **2018**, *7*, e35560.

# Supporting Information: Solvent Effects on the Menshutkin Reaction

Haydar T. Turan,<sup>†</sup> Sebastian Brickel,<sup>‡</sup> and Markus Meuwly<sup>\*,†</sup>

<sup>†</sup>*Department of Chemistry, University of Basel, Klingelbergstrasse 80, Basel, Switzerland*

<sup>‡</sup>*Department of Chemistry, University of Basel, Klingelbergstrasse 80, Basel, Switzerland*

*Present Address: Department of Chemistry - BMC, Uppsala University, BMC Box 576,  
751 23 Uppsala, Sweden*

E-mail: m.meuwly@unibas.ch

## Abstract

Table S1: The harmonic bond, Morse bond, angle and generalised van der Waals (GVDW) parameters for for  $\text{NH}_3 + \text{MeCl}$ .  $K_b$  in kcal/mol/ $\text{\AA}^2$ ,  $d_{\text{eq}}$  in  $\text{\AA}$ ,  $D_e$  in kcal/mol,  $d_{\text{eq}}$  in  $\text{\AA}$ ,  $\beta$  in  $\text{\AA}^{-1}$ ,  $K_\theta$  in kcal/mol/radian<sup>2</sup>,  $r$  in  $\text{\AA}$  and  $\epsilon$  in kcal/mol.

	Reactant		Product	
Bond Harmonic	$K_b$	$d_{\text{eq}}$	$K_b$	$d_{\text{eq}}$
N – H <sub>NH<sub>3</sub></sub>	437.150	1.016	490.522	1.039
C – H <sub>Me</sub>	375.145	1.100	369.812	1.151
Bond Morse	$D_e$	$d_{\text{eq}}$	$\beta$	
C – Cl	145.720	1.785	0.582	
C – N	47.9544	1.520	1.682	
	Reactant		Product	
Angle	$K_\theta$	$\Theta_{\text{eq}}$	$K_\theta$	$\Theta_{\text{eq}}$
H <sub>NH<sub>3</sub></sub> – N – H <sub>NH<sub>3</sub></sub>	40.594	107.500	44.274	108.806
H <sub>Me</sub> – C – H <sub>Me</sub>	37.170	110.010	21.686	114.437
H <sub>Me</sub> – C – Cl	45.335	112.040	X	X
H <sub>NH<sub>3</sub></sub> – N – C	X	X	57.420	107.189
H <sub>NH<sub>3</sub></sub> – C – H <sub>Me</sub>	X	X	25.311	105.421
GVDW	$r$	$\epsilon$	$n$	$m$
Reactant (N–C)	1.209	0.115	6.232	12.323
Product (C–Cl)	2.500	0.300	5.518	12.196

Table S2: The harmonic bond, Morse bond, angle and generalised van der Walls (GVDW) parameters for for Pyr+MeBr.  $K_b$  in kcal/mol/Å<sup>2</sup>,  $d_{eq}$  in Å,  $D_e$  in kcal/mol,  $d_{eq}$  in Å,  $\beta$  in Å<sup>-1</sup>,  $K_\theta$  in kcal/mol/radian<sup>2</sup>,  $r$  in Å and  $\epsilon$  in kcal/mol.

	Reactant		Product	
Bond Harmonic	$K_b$	$d_{eq}$	$K_b$	$d_{eq}$
C <sub>Pyr</sub> – C <sub>Pyr</sub>	389.240	1.369	420.800	1.393
C <sub>Pyr</sub> – N <sub>Pyr</sub>	446.700	1.319	464.880	1.345
C <sub>Pyr</sub> – H <sub>Pyr</sub>	352.560	1.083	246.970	1.078
C <sub>Me</sub> – H <sub>Me</sub>	293.370	1.083	226.040	1.074
Bond Morse	$D_e$	$d_{eq}$	$\beta$	
C – Br	87.908	1.972	0.957	
C – N	286.170	1.581	0.908	
	Reactant		Product	
Angle	$K_\theta$	$\Theta_{eq}$	$K_\theta$	$\Theta_{eq}$
C <sub>Pyr</sub> – C <sub>Pyr</sub> – H <sub>Pyr</sub>	29.657	122.100	27.082	120.800
C <sub>Pyr</sub> – C <sub>Pyr</sub> – N <sub>Pyr</sub>	39.676	126.390	37.792	121.650
N <sub>Pyr</sub> – C <sub>Pyr</sub> – H <sub>Pyr</sub>	43.001	118.010	52.771	115.520
C <sub>Pyr</sub> – N <sub>Pyr</sub> – C <sub>Pyr</sub>	81.961	112.800	96.761	119.040
H <sub>Me</sub> – C <sub>Me</sub> – H <sub>Me</sub>	30.810	104.220	32.760	115.190
H <sub>Me</sub> – C <sub>Me</sub> – Br	40.252	102.410	X	X
N <sub>Pyr</sub> – C <sub>Me</sub> – H <sub>Me</sub>	X	X	48.194	104.190
C <sub>Pyr</sub> – N <sub>Pyr</sub> – H <sub>Me</sub>	X	X	40.800	121.640
GVDW	$r$	$\epsilon$	$n$	$m$
Reactant (N–C)	1.296	0.751	8.096	16.710
Product (C–Br)	0.491	0.927	7.773	11.510

Table S3: GAPO parameters for NH<sub>3</sub>+MeCl:  $i$  labels the reactant,  $j$  labels the product,  $V_{ij,k}^0$  is the center of each of the  $k = 3$  Gaussian functions (in kcal/mol),  $\sigma_{ij,k}$  is the width of each Gaussian (in kcal/mol) and  $\alpha_{ij,k0}$  is the polynomial coefficient. In the present case polynomial order “0” was sufficient, hence  $\alpha_{ij,k0}$ .

$k$	$V_{ij,k}^0$	$\sigma_{ij,k}$	$\alpha_{ij,k0}$
1	0.48578	22.15304	-17.47731
2	40.88660	12.45761	-1.34837
3	-36.67239	11.02057	-1.014567

Table S4: GAPO parameters for Pyr+MeBr:  $i$  labels the reactant,  $j$  labels the product,  $V_{ij,k}^0$  is the center of the Gaussian function (in kcal/mol), and  $\sigma_{ij,k}$  the width of the Gaussian (in kcal/mol).  $\alpha_{ij,k0}$  is the polynomial coefficient in kcal/mol. In the present case polynomial order “0” was sufficient, hence  $\alpha_{ij,k0}$ .

$k$	$V_{ij,k}^0$	$\sigma_{ij,k}$	$\alpha_{ij,k0}$
1	-44.46610	12.24875	-0.747557
2	1.17231	28.18915	-22.93224
3	55.29621	23.35329	-3.89254

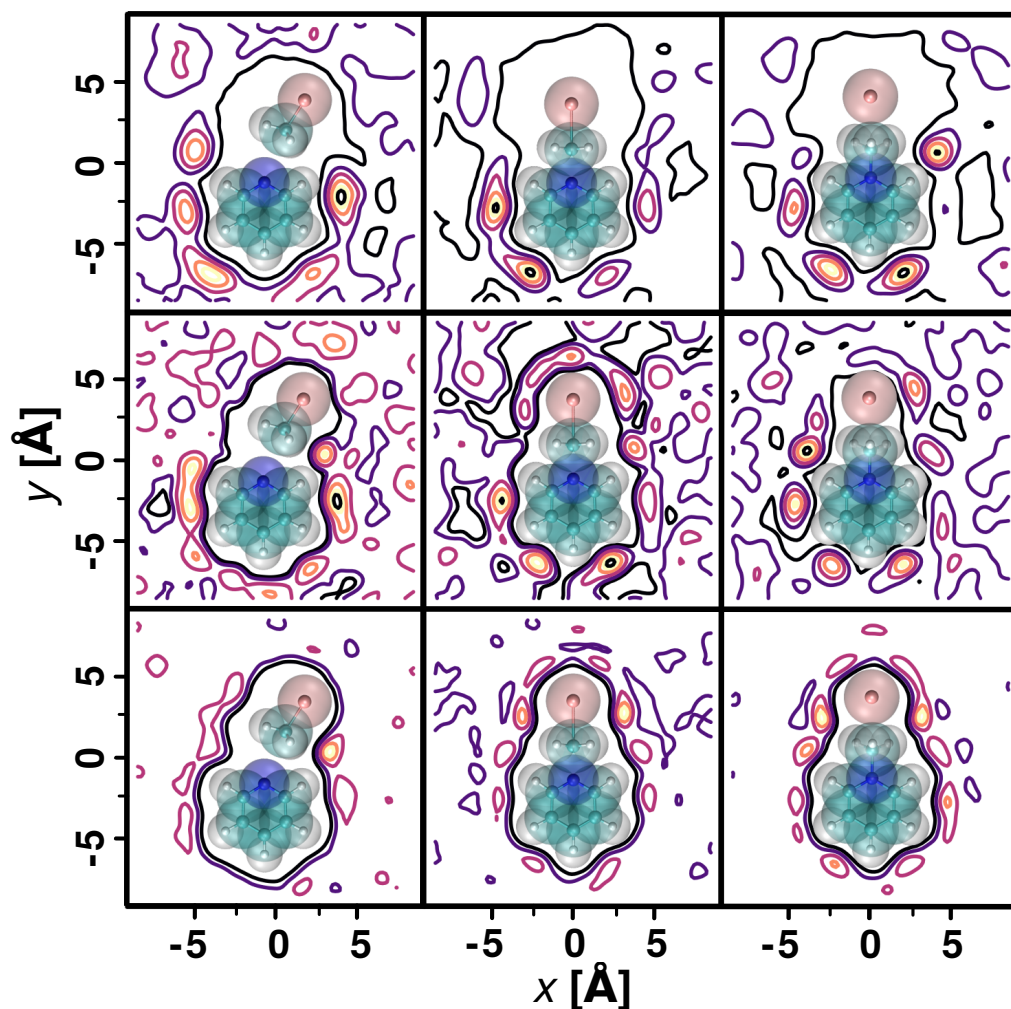


Figure S1: 2-dimensional solvent distributions for Pyr+MeBr from 2 ns simulations in polar solvents: acetonitrile, methanol and water (from top to bottom) around the reactant, TS, and product state structures of the solute (from left to right) projected onto the  $xy$ -plane containing the chloride, carbon and nitrogen atoms. Units in Å. In the simulations and the figure the solute is in its optimized structure for the reactant, TS, and product state, respectively, at the MP2/6-311++G(2d,2p) level of theory. The color code for atoms is H (white), C (cyan), N (blue) and Br (pink).

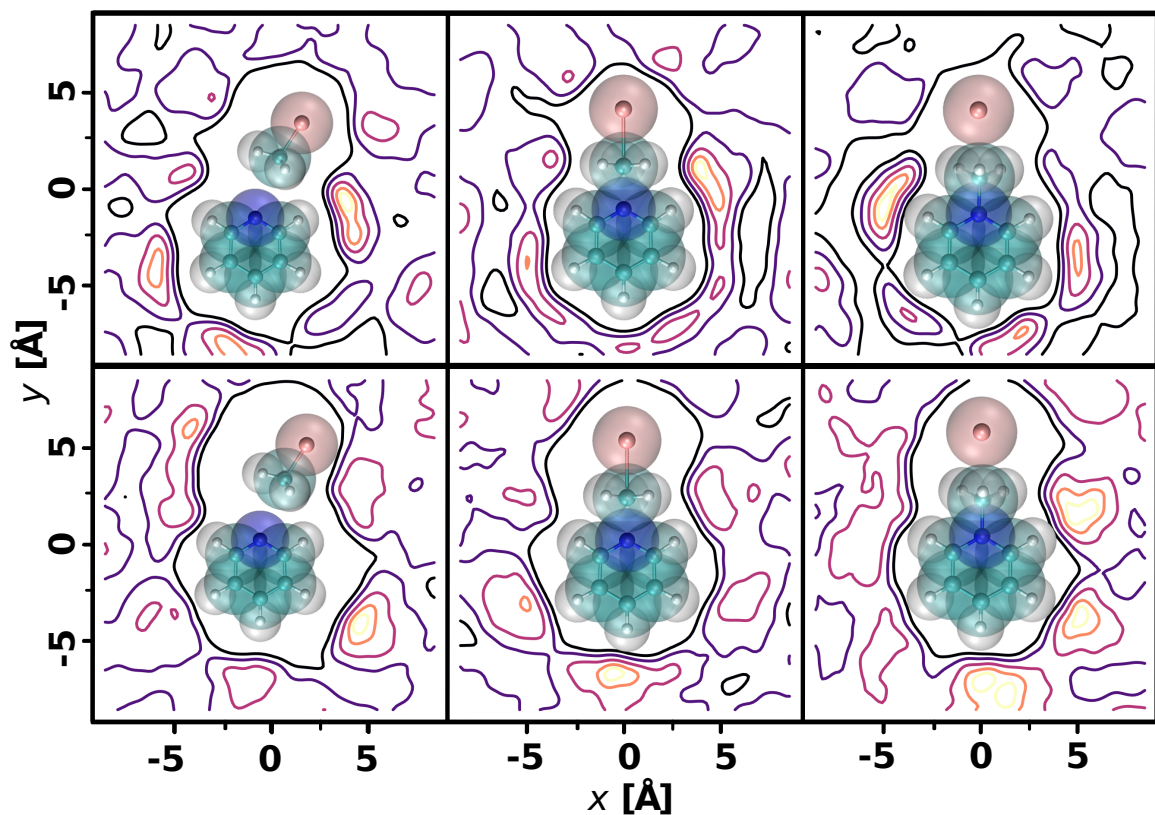


Figure S2: 2-dimensional solvent distributions for Pyr+MeBr in apolar solvents: benzene (top) and hexane (bottom) around the reactant, TS, and product state structures of the solute (from left to right) projected onto the  $xy$ -plane containing the chloride, carbon and nitrogen atoms. Units in Å. In the simulations and the figure the solute is in its optimized structure for the reactant, TS, and product state, respectively, at the MP2/6-311++G(2d,2p) level of theory. The color code for atoms is H (white), C (cyan), N (blue) and Br (pink).



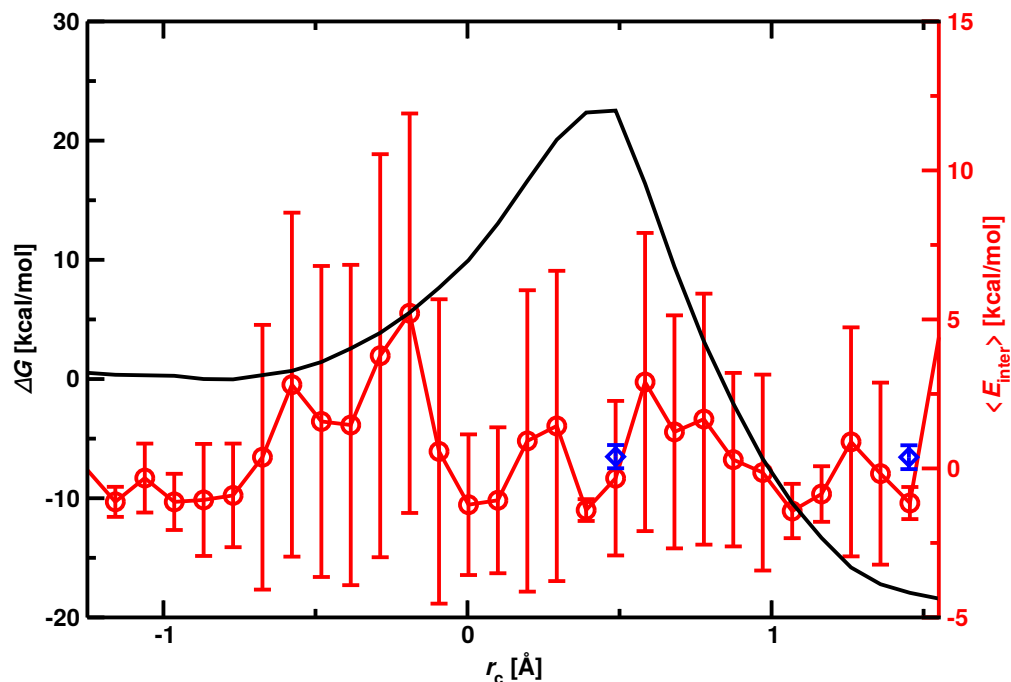


Figure S3: Potentials of mean force for Pyr+MeBr in methanol (black line) and the average solvent-solvent interaction for molecules 5Å around the solute in kcal/mol/molecule (red line). The circles are the mean for a given umbrella together with the standard deviation from the mean (fluctuation bar). The blue diamonds are average solvent-solvent interaction energies for molecules 5Å around the solute in kcal/mol/molecule from 2 ns *NVT* simulations in reactant, TS and product states, respectively, together with the standard deviation (fluctuation bar).

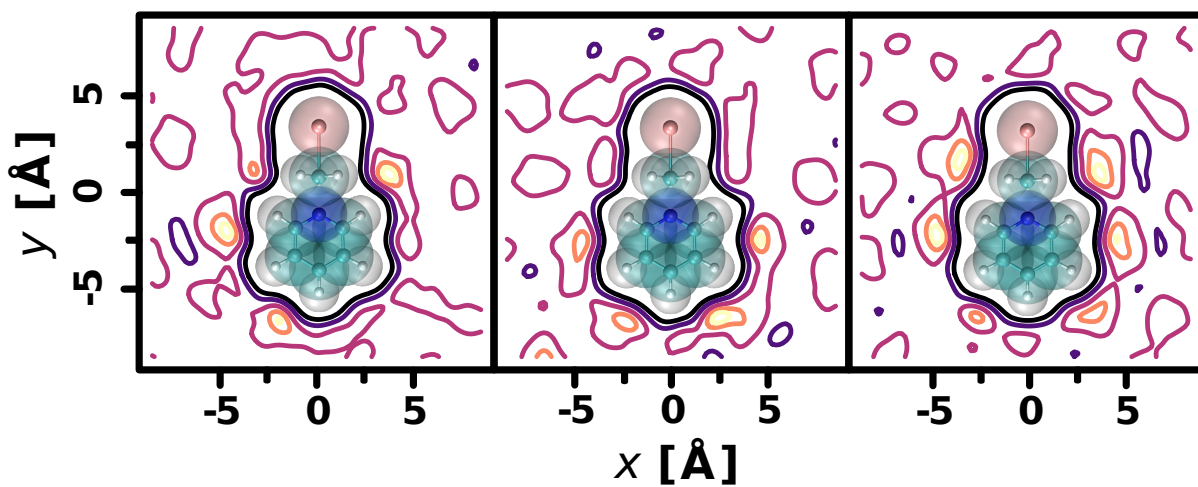


Figure S4: 2-dimensional solvent distribution for Pyr+MeBr in methanol for  $r_c = [-0.3, -0.2, -0.1]$  projected onto the  $xy$ -plane, respectively. The color code for atoms is H (white), C (cyan), N (blue) and Br (pink).